Eur. Phys. J. C 20, 401–430 (2001)
Digital Object Identifier (DOI) 10.1007/s100520100689

THE EUROPEAN PHYSICAL JOURNAL C

Measurement of the Tau Polarisation at LEP

The ALEPH Collaboration

A. Heister, S. Schael
Physikalisches Institut das RWTH-Aachen, 52056 Aachen, Germany

R. Barate, I. De Bonis, D. Decamp, P. Ghez, C. Goy, J.-P. Lees, E. Merle, M.-N. Minard, B. Pietrzyk
Laboratoire de Physique des Particules (LAPP), IN^{2}P^3-CNRS, 74019 Annecy-le-Vieux Cedex, France

R. Alemany, S. Bravo, M.P. Casado, M. Chmeissani, J.M. Crespo, E. Fernandez, M. Fernandez-Bosman, Ll. Garrido[15], E. Graugés, M. Martinez, G. Merino, R. Miquel, Ll.M. Mir, A. Pacheco, H. Ruiz
Institut de Física d'Altes Energies, Universitat Autònoma de Barcelona, 08193 Bellaterra (Barcelona), Spain[7]

A. Colaleo, D. Creanza, M. de Palma, G. Iaselli, G. Maggi, M. Maggi[1], S. Nuzzo, A. Ranieri, G. Raso[23], F. Ruggieri, G. Selvaggi, L. Silvestris, P. Tempesta, A. Tricomi[3], G. Zito
Dipartimento di Fisica, INFN Sezione di Bari, 70126 Bari, Italy

X. Huang, J. Lin, Q. Ouyang, T. Wang, Y. Xie, R. Xu, S. Xue, J. Zhang, L. Zhang, W. Zhao
Institute of High Energy Physics, Academia Sinica, Beijing, P.R. China[8]

D. Abbaneo, P. Azzurri, G. Boix[6], O. Buchmüller, M. Cattaneo, F. Cerutti, B. Clerbaux, G. Dissertori, H. Drevermann, R.W. Forty, M. Frank, T.C. Greening, J.B. Hansen, J. Harvey, P. Janot, B. Jost, M. Kado, P. Mato, A. Moutoussi, F. Ranjard, L. Rolandi, D. Schlatter, M. Schmitt[27], O. Schneider[2], P. Spagnolo, W. Tejessy, F. Teubert, E. Tournefier[25], J. Ward, A.E. Wright
European Laboratory for Particle Physics (CERN), 1211 Geneva 23, Switzerland

Z. Ajaltouni, F. Badaud, A. Falvard[22], P. Gay, P. Henrard, J. Jousset, B. Michel, S. Monteil, J-C. Montret, D. Pallin, P. Perret, F. Podlyski
Laboratoire de Physique Corpusculaire, Université Blaise Pascal, IN^{2}P^3-CNRS, Clermont-Ferrand, 63177 Aubière, France

J.D. Hansen, J.R. Hansen, P.H. Hansen, B.S. Nilsson, A. Wäänänen
Niels Bohr Institute, 2100 Copenhagen, Denmark[9]

G. Daskalakis, A. Kyriakis, C. Markou, E. Simopoulou, A. Vayaki
Nuclear Research Center Demokritos (NRCD), 15310 Attiki, Greece

A. Blondel[12], G. Bonneaud, J.-C. Brient, A. Rougé, M. Rumpf, M. Swynghedauw, M. Verderi, H. Videau
Laboratoire de Physique Nucléaire et des Hautes Energies, Ecole Polytechnique, IN^{2}P^3-CNRS, 91128 Palaiseau Cedex, France

E. Focardi, G. Parrini, K. Zachariadou
Dipartimento di Fisica, Università di Firenze, INFN Sezione di Firenze, 50125 Firenze, Italy

A. Antonelli, M. Antonelli, G. Bencivenni, G. Bologna[4], F. Bossi, P. Campana, G. Capon, V. Chiarella, P. Laurelli, G. Mannocchi[5], F. Murtas, G.P. Murtas, L. Passalacqua, M. Pepe-Altarelli[24]
Laboratori Nazionali dell'INFN (LNF-INFN), 00044 Frascati, Italy

A.W. Halley, J.G. Lynch, P. Negus, V. O'Shea, C. Raine, A.S. Thompson
Department of Physics and Astronomy, University of Glasgow, Glasgow G12 8QQ, UK[10]

S. Wasserbaech
Department of Physics, Haverford College, Haverford, PA 19041-1392, USA

R. Cavanaugh, S. Dhamotharan, C. Geweniger, P. Hanke, G. Hansper, V. Hepp, E.E. Kluge, A. Putzer, J. Sommer, K. Tittel, S. Werner[19], M. Wunsch[19]
Kirchhoff-Institut für Physik, Universität Heidelberg, 69120 Heidelberg, Germany[16]

R. Beuselinck, D.M. Binnie, W. Cameron, P.J. Dornan, M. Girone[1], N. Marinelli, J.K. Sedgbeer, J.C. Thompson[14]
Department of Physics, Imperial College, London SW7 2BZ, UK[10]

V.M. Ghete, P. Girtler, E. Kneringer, D. Kuhn, G. Rudolph
Institut für Experimentalphysik, Universität Innsbruck, A-6020 Innsbruck, Austria[18]

E. Bouhova-Thacker, C.K. Bowdery, A.J. Finch, F. Foster, G. Hughes, R.W.L. Jones[1], M.R. Pearson, N.A. Robertson
Department of Physics, University of Lancaster, Lancaster LA1 4YB, UK[10]

I. Giehl, K. Jakobs, K. Kleinknecht, G. Quast, B. Renk, E. Rohne, H.-G. Sander, H. Wachsmuth, C. Zeitnitz
Institut für Physik, Universität Mainz, 55099 Mainz, Germany[16]

A. Bonissent, J. Carr, P. Coyle, O. Leroy, P. Payre, D. Rousseau, M. Talby
Centre de Physique des Particules, Université de la Méditerranée, IN^{2}P^3-CNRS, 13288 Marseille, France

M. Aleppo, F. Ragusa
Dipartimento di Fisica, Università di Milano e INFN Sezione di Milano, 20133 Milano, Italy

A. David, H. Dietl, G. Ganis[26], K. Hüttmann, G. Lütjens, C. Mannert, W. Männer, H.-G. Moser, R. Settles[1], H. Stenzel, W. Wiedenmann, G. Wolf
Max-Planck-Institut für Physik, Werner-Heisenberg-Institut, 80805 München, Germany[p]

J. Boucrot[1], O. Callot, S. Chen, M. Davier, L. Duflot, J.-F. Grivaz, Ph. Heusse, A. Jacholkowska[22], J. Lefrançois, I. Nikolic, J.-J. Veillet, I. Videau, C. Yuan
Laboratoire de l'Accélérateur Linéaire, Université de Paris-Sud, IN^{2}P^3-CNRS, 91898 Orsay Cedex, France

G. Bagliesi, T. Boccali, G. Calderini, V. Ciulli, L. Foà, A. Giassi, F. Ligabue, A. Messineo, F. Palla, G. Sanguinetti, A. Sciabà, G. Sguazzoni, R. Tenchini[1], A. Venturi, P.G. Verdini
Dipartimento di Fisica dell'Università, INFN Sezione di Pisa, e Scuola Normale Superiore, 56010 Pisa, Italy

G.A. Blair, G. Cowan, M.G. Green, T. Medcalf, J.A. Strong, P. Teixeira-Dias, J.H. von Wimmersperg-Toeller
Department of Physics, Royal Holloway & Bedford New College, University of London, Egham, Surrey TW20 OEX, UK[10]

R.W. Clifft, T.R. Edgecock, P.R. Norton, I.R. Tomalin
Particle Physics Dept., Rutherford Appleton Laboratory, Chilton, Didcot, Oxon OX11 OQX, UK[10]

B. Bloch-Devaux[1], P. Colas, S. Emery, W. Kozanecki, E. Lançon, M.-C. Lemaire, E. Locci, P. Perez, J. Rander, J.-F. Renardy, A. Roussarie, J.-P. Schuller, J. Schwindling, A. Trabelsi[21], B. Vallage
CEA, DAPNIA/Service de Physique des Particules, CE-Saclay, 91191 Gif-sur-Yvette Cedex, France[17]

N. Konstantinidis, A.M. Litke, G. Taylor
Institute for Particle Physics, University of California at Santa Cruz, Santa Cruz, CA 95064, USA[13]

C.N. Booth, S. Cartwright, F. Combley, M. Lehto, L.F. Thompson
Department of Physics, University of Sheffield, Sheffield S3 7RH, UK[10]

K. Affholderbach, A. Böhrer, S. Brandt, C. Grupen, A. Misiejuk, A. Ngac, G. Prange, U. Sieler
Fachbereich Physik, Universität Siegen, 57068 Siegen, Germany[16]

G. Giannini
Dipartimento di Fisica, Università di Trieste e INFN Sezione di Trieste, 34127 Trieste, Italy

J. Rothberg
Experimental Elementary Particle Physics, University of Washington, Seattle, WA 98195 USA

S.R. Armstrong, K. Cranmer, P. Elmer, D.P.S. Ferguson, Y. Gao[20], S. González, O.J. Hayes, H. Hu, S. Jin, J. Kile, P.A. McNamara III, J. Nielsen, W. Orejudos, Y.B. Pan, Y. Saadi, I.J. Scott, J. Walsh, Sau Lan Wu, X. Wu, G. Zobernig
Department of Physics, University of Wisconsin, Madison, WI 53706, USA[11]

Received: 2 March 2001 /
Published online: 8 June 2001 – © Springer-Verlag / Società Italiana di Fisica 2001

Abstract. The polarisation of τ's produced in Z decay is measured using 160 pb^{-1} of data accumulated at LEP by the ALEPH detector between 1990 and 1995. The variation of the polarisation with polar angle yields the two parameters $\mathcal{A}_e = 0.1504 \pm 0.0068$ and $\mathcal{A}_\tau = 0.1451 \pm 0.0059$ which are consistent with the hypothesis of e-τ universality. Assuming universality, the value $\mathcal{A}_{e\text{-}\tau} = 0.1474 \pm 0.0045$ is obtained from which the effective weak mixing angle $\sin^2\theta_{\rm W}^{\rm eff} = 0.23147 \pm 0.00057$ is derived.

1 Introduction

Owing to parity violation in Z production and decay, the τ leptons produced in the $e^+e^- \to \mathrm{Z} \to \tau^+\tau^-$ reaction are polarised. Except for very small $\mathcal{O}(m_\tau^2/m_Z^2)$ corrections, the τ^+ and τ^- have opposite helicities, hence opposite polarisations. In the present paper, P_τ is defined as the τ^- polarisation.

The P_τ dependence on the angle θ formed by the τ^- direction and the e^- beam is given, in the improved Born approximation at the Z peak, by

$$P_\tau(\cos\theta) = -\frac{\mathcal{A}_\tau(1+\cos^2\theta) + \mathcal{A}_e(2\cos\theta)}{(1+\cos^2\theta) + \frac{4}{3}\mathcal{A}_{fb}(2\cos\theta)}, \qquad (1)$$

where $\mathcal{A}_{fb}$ is the forward-backward charge asymmetry of τ production and

$$\mathcal{A}_l \equiv 2g_V^l g_A^l/[(g_V^l)^2 + (g_A^l)^2]. \qquad (2)$$

In the standard model, the vector (g_V^l) and axial vector (g_A^l) couplings of the Z to lepton l are independent of the lepton flavour and related to the effective weak mixing angle by

$$g_V^l/g_A^l = 1 - 4\sin^2\theta_W^{eff}. \qquad (3)$$

Therefore, the measurement of $P_\tau(\cos\theta)$ allows a test of the e-τ universality prediction $\mathcal{A}_\tau = \mathcal{A}_e$ and, assuming universality, gives a determination of the weak mixing angle.

The analyses presented here use the complete set of data (160 pb^{-1}) accumulated by the ALEPH detector at LEP I from 1990 to 1995. They supersede the previously published results [1–3].

The τ polarisation is extracted from five decay channels which amount to a total branching ratio of about 90%, namely $\tau \to e\nu\bar{\nu}$, $\tau \to \mu\nu\bar{\nu}$, $\tau \to \pi\nu$, $\tau \to \rho\nu$, $\tau \to a_1\nu$. The channels $\tau \to K\nu$ and $\tau \to K\pi^0\nu$ are included in $\tau \to \pi\nu$ and $\tau \to \rho\nu$ respectively, and the a_1 decay is observed as both $a_1 \to \pi^+\pi^-\pi^\pm$ $(3h)$ and $a_1 \to \pi^0\pi^0\pi^\pm$ $(h2\pi^0)$.

The methods employed for the P_τ measurement in each channel are described in the following section. At each energy, a fit of (1) allows to determine uncorrected

[1] Also at CERN, 1211 Geneva 23, Switzerland
[2] Now at Université de Lausanne, 1015 Lausanne, Switzerland
[3] Also at Dipartimento di Fisica di Catania and INFN Sezione di Catania, 95129 Catania, Italy
[4] Deceased
[5] Also Istituto di Cosmo-Geofisica del C.N.R., Torino, Italy
[6] Supported by the Commission of the European Communities, contract ERBFMBICT982894
[7] Supported by CICYT, Spain
[8] Supported by the National Science Foundation of China
[9] Supported by the Danish Natural Science Research Council
[10] Supported by the UK Particle Physics and Astronomy Research Council
[11] Supported by the US Department of Energy, grant DE-FG0295-ER40896
[12] Now at Departement de Physique Corpusculaire, Université de Genève, 1211 Genève 4, Switzerland
[13] Supported by the US Department of Energy, grant DE-FG03-92ER40689
[14] Also at Rutherford Appleton Laboratory, Chilton, Didcot, UK
[15] Permanent address: Universitat de Barcelona, 08208 Barcelona, Spain
[16] Supported by the Bundesministerium für Bildung, Wissenschaft, Forschung und Technologie, Germany
[17] Supported by the Direction des Sciences de la Matière, C.E.A
[18] Supported by the Austrian Ministry for Science and Transport
[19] Now at SAP AG, 69185 Walldorf, Germany
[20] Also at Department of Physics, Tsinghua University, Beijing, The People's Republic of China
[21] Now at Département de Physique, Faculté des Sciences de Tunis, 1060 Le Belvédère, Tunisia
[22] Now at Groupe d' Astroparticules de Montpellier, Université de Montpellier II, 34095 Montpellier, France
[23] Also at Dipartimento di Fisica e Tecnologie Relative, Università di Palermo, Palermo, Italy
[24] Now at CERN, 1211 Geneva 23, Switzerland
[25] Now at ISN, Institut des Sciences Nucléaires, 53 Av. des Martyrs, 38026 Grenoble, France
[26] Now at INFN Sezione di Roma II, Dipartimento di Fisica, Universitá di Roma Tor Vergata, 00133 Roma, Italy
[27] Now at Harvard University, Cambridge, MA 02138, USA

Table 1. Ideal sensitivities for the polarisation measurement in the τ decay channels without and with the τ direction $\vec{\tau}$ [5]. The sensitivity is defined as $S = 1/\Delta\sqrt{N}$, where Δ is the statistical error expected for a sample of N events

Channel	Sensitivity	
	without $\vec{\tau}$	with $\vec{\tau}$
$\pi\nu$	0.58	0.58
$\rho\nu$	0.49	0.58
$a_1\nu$	0.45	0.58
$l\nu\bar{\nu}$	0.22	–

parameters A_τ and A_e. Final corrections are needed to get the effective couplings at the Z, whose combinations $2g_V^l g_A^l/[(g_V^l)^2 + (g_A^l)^2]$ are written $\mathcal{A}_l$ to distinguish them from the uncorrected A_l. They are computed with the help of the ZFITTER program [4].

2 Methods for τ polarisation measurement

2.1 Information from a polarised τ decay

The general method to measure the τ polarisation in an optimal way [5] takes advantage of the linear dependence on the polarisation of the distribution of decay products.

In each decay channel, the decay products are described by a set of n observables $\boldsymbol{\xi}$ and their distribution reads

$$W(\boldsymbol{\xi}) = f(\boldsymbol{\xi}) + P_\tau g(\boldsymbol{\xi}), \tag{4}$$

with the normalization and positivity conditions:

$$\int f(\boldsymbol{\xi}) d^n\boldsymbol{\xi} = 1, \quad \int g(\boldsymbol{\xi}) d^n\boldsymbol{\xi} = 0, \ f \geq 0, \text{ and } |g| \leq f.$$

With the optimal variable for the channel defined by

$$\omega = \frac{g(\boldsymbol{\xi})}{f(\boldsymbol{\xi})}, \tag{5}$$

the distribution in (4) can be cast, with no loss of information, in the general reduced form

$$\begin{aligned} \hat{W}(\omega) &= \hat{f}(\omega)\,[1 + P_\tau\,\omega] \\ &= \frac{1}{2}\left[(1+P_\tau)\hat{W}^+(\omega) + (1-P_\tau)\hat{W}^-(\omega)\right], \end{aligned} \tag{6}$$

where W^+ and W^- are the distributions for positive and negative helicity respectively.

For events in which both τ's decay into hadrons, it is possible to get information on the line of flight of the two τ's [6]. It is shown in [5] that, in an ideal measurement, using the knowledge of the τ direction to construct the ω variable gives for ρ and a_1 decays the same sensitivity as that for π decay (Table 1).

The polarisation is obtained by means of a fit of $\hat{W}^+(\omega)$ and $\hat{W}^-(\omega)$ functions to the experimental $\hat{W}(\omega)$ distribution. The $W^\pm$ functions are constructed from Monte Carlo events and normalized to the acceptances. Non-tau background is taken into account in the fit.

The validity of the standard model for the description of τ decays has been checked elsewhere [7] by the measurement of the τ decay parameters.

In the standard model, which is assumed here, the decay distributions for the $\tau \to l\nu\bar{\nu}$, $\tau \to \pi\nu$, and $\tau \to \rho\nu$ channels are completely determined by Lorentz invariance and there is no hadronic decay model dependence in the definition of ω. Furthermore, because the τ polarisation always appears through the product χP, where χ is the handedness of the neutrino [2], the definition of the ω variable is the same for τ^+ and τ^-, as are its distributions when expressed in terms of the τ^- polarisation $P_\tau = P_{\tau^-} = -P_{\tau^+}$.

The situation is more intricate in the case of the a_1 decay. There, in addition to the decay angles, the two-pion masses are required to describe the hadronic system. Their dependence is embodied in four "structure functions", W_A, W_C, W_D, and W_E [8], whose computation requires a model of the a_1 decay. The model [8] that is used in the present study assumes a sequential $a_1 \to \rho\pi$ decay. The sign of the W_E function depends on the charge of the τ so that the expression of the ω variable is not exactly the same for τ^+ and τ^-.

For the $\tau \to l\nu\bar{\nu}$ and $\tau \to \pi\nu$ decay modes, the optimal variable is the ratio $x = E/E_{\text{beam}}$ of the energy of the charged particle (l or π) to the beam energy.

For the other channels, the τ decay is described by one angle and the mass of the hadronic system. The subsequent decay of the hadron is described by two angles in the case of the ρ, and by two effective masses and three Euler angles in the case of the a_1. If the τ direction is not available, one of the angles used to describe the hadron decay is not measurable and the analytical form of the decay distributions is made more complex by the Wigner rotation between the laboratory and τ rest frame helicity axes. The expressions used for the construction of the ω variables can be found in [2] and [8].

Although all the information relevant to the polarisation measurement is contained in the sole ω variable, the distributions of the other parameters are useful when checking the quality of the simulations and the understanding of energy calibrations. For example, the two angles used to describe the $\tau \to \rho\nu$ decay when the τ direction is not available are [2] $\cos\psi_\tau \propto (2(E_{\pi^\pm} + E_{\pi^0})/E_{\text{beam}} - 1)$ and $\cos\psi_\rho \propto (E_{\pi^\pm} - E_{\pi^0})/(E_{\pi^\pm} + E_{\pi^0})$. The comparison of their distributions in data and Monte Carlo is the best test of the quality of the measurement.

2.2 The analyses

Two complementary analyses have been performed, which emphasize differently the sensitivity of the estimators and the reduction of the systematic uncertainties.

In the first one, the information from the opposite hemisphere of the event is used for background rejection when studying a τ decay. This approach, which was followed in previous analyses [1–3], is called hereafter the

"single τ method". In this method, the information exploited to construct the ω variable comes from only one of the two hemispheres defined by the plane perpendicular to the thrust axis.

As mentioned in the previous section, for events in which both τ's decay into hadrons it is possible to get information on the line of flight of the two τ's and construct an ω variable giving an improved sensitivity for the $\tau \to \rho\nu$ and $\tau \to a_1\nu$ decays. This more global approach is followed in the second analysis and is called hereafter the "τ direction method".

These two methods use the same set of data and many common standard ALEPH tools. The two analyses have nevertheless been performed independently and thus are described in detail in Sects. 4 and 5. The combination of their results is presented in Sect. 6.

3 Detector and data sets

3.1 The ALEPH detector

The ALEPH detector and its performance are described elsewhere [9,10]. The study of τ polarisation requires a very special care in the alignment and calibration procedures to master the differences between real and simulated data at the required level.

The charged track measurement rests on three elements, the Vertex Detector (VDET), the Inner Tracking Chamber (ITC), and the Time Projection Chamber (TPC).

The VDET, a double-sided silicon strip detector, provides precise measurements close to the interaction point and, therefore, plays an important role in determining the τ direction.

The ITC is a drift chamber with wires parallel to the beam and a short drift time. Besides providing a trigger, it is an efficient tool against cosmic rays. Because its complete drift time is about 200 ns, to be compared to the 11 μs interval between bunch collisions, its sensitive time window is small. Therefore, there are few if any ITC hits in most triggers on cosmic rays. If present, they are not reconstructed with the correct timing and the reconstructed track is distorted leading to erroneous distances of approach to the interaction point.

The TPC is a very large volume drift chamber. Together with the VDET and ITC, it brings a resolution on the track momentum which reaches $6 \times 10^{-4} p$ (p in GeV), but to get this accuracy a precise calibration is needed. For these analyses, the distortions from the TPC are derived from the study of nonradiative $\mu^+\mu^-$ events in ϕ and $\cos\theta$ bins, where ϕ and θ are the azimuthal and polar angle of the μ^- with respect to the e^- beam. The departures from the corresponding observations on Monte Carlo are corrected for, considering that the distortions on the sum of positive and negative track momenta are due to field effects and that the distortions on the difference are due to sagitta measurement effects, i.e. alignment effects.

Apart from momentum and angle measurements, the tracking system is used to measure the impact parameter relative to the beam axis, denoted d_0.

The tracking detectors are surrounded by the electromagnetic calorimeter (ECAL). All these elements are installed inside a superconducting coil which provides a 1.5 T axial field. The return yoke of the magnetic field is instrumented to form a hadron calorimeter (HCAL).

The ECAL is a lead/proportional wire chamber sampling device of 22 radiation length thickness. The insensitive regions between its modules (cracks) represent 2% of the barrel and 6% of the endcap areas. The anode wire signal is read plane by plane. The cathodes are divided in pads, making 74,000 towers pointing to the interaction point. These towers are read out in three sections in depth ("storeys"or "stacks"). The use of the energies measured with the pad towers is mandatory whenever a precise direction is needed but, in the case of τ events, the energy collected on the wires may be advantageous. It does not suffer from disconnected channels ensuring that the total energy left in each module is properly known. This comes from the fact that the lack of a plane is, to first order, corrected for by the energy calibration. It has a very low level of noise (about 10 MeV for a complete module). The energy resolution therefore does not suffer from threshold effects and is slightly better than the resolution of the pad signal. Another interesting feature is that the 45 plane signals provide a complete depth profile of the energy deposit.

The calibration of the ECAL was performed independently in the two analyses presented below but the salient features are common and the technique is the same for pad and wire signals. First a correction map is applied which takes care of local gain variations related to mechanical distortions, then gain dependencies as a function of ϕ and θ are applied to each module, finally the modules are inter-calibrated and normalized to the response observed in Monte Carlo. A problem in this procedure comes from the nonlinearity with energy of the calorimeter response which reaches 4% at 50 GeV. Bhabha events provide a calibration at the beam energy but not a measurement of the nonlinearity which can be parametrized in first order by a constant α in the expression giving the true energy as a function of the measured one, $E_t = E_m(1+\alpha E_m)$. To extract α, clean electrons are selected and the E/p ratio is compared, as a function of energy, between real data and Monte Carlo where the saturation effects have not been simulated. This is done independently for barrel and endcaps.

The HCAL is made of 23 layers of streamer tubes inserted between 5 cm thick iron plates. The individual tube hits are recorded digitally and the energy is read out in 4,788 projective towers. This calorimeter is used primarily for discriminating between pions and muons. This does not require a specific energy calibration. For the current purpose, use is made essentially of the digital pattern provided by the firing of the streamer tubes. In particular, the pattern recognition described in [2] is used to get variables describing the shape of the shower.

The HCAL is surrounded by two double layers of streamer tubes, the muon chambers, providing additional information for muon identification.

The luminosity calorimeters are not utilized in the analyses presented here.

3.2 The data and Monte Carlo samples

The data used in these analyses were accumulated with the ALEPH detector during the years 1990 to 1995 at centre-of-mass energies close to the Z mass. This set, often referred to as the LEP I data set, corresponds to about 160 pb^{-1} of data. A detailed description of the characteristics of each period can be found in [11]. For the present study no requirement on the luminosity measurement quality is made.

Monte Carlo simulation samples were generated for the $\tau^+\tau^-$ events as well as for the different backgrounds through the complete detector simulation chain. A sample of 1.9×10^6 $\tau^+\tau^-$ events was generated using KORALZ [12]. For each year and energy of data taking a sample of about six times the real data sample was simulated with the same energy and the effective detector geometry of the year.

A $\mu^+\mu^-$ sample of about $4{\times}10^5$ events was simulated using also KORALZ for different years and energies. About $5{\times}10^5$ large angle Bhabha events were produced using UNIBAB [13], and some with BABAMC [14], for different energies. For the two-photon interaction processes, the simulation used the generator PHOT02 [15]. Finally the four-fermion processes $\ell^+\ell^-\mathrm{V}$, defined [11] as a pair of leptons associated with a two particle system (V) of lower mass, were generated using FERMISV [16].

4 Single τ analysis

4.1 Introduction

The aim of this analysis is to reduce the systematic uncertainties, even at the price of some inefficiency. Data have been processed separately for each year of LEP operation in order to take as much care as possible of time-variations in the behaviour of the detector.

Particle and channel identification, as well as non-τ background rejection, are achieved by means of likelihood estimators, in order to optimize the efficiencies. These estimators are constructed from Monte Carlo distributions of the relevant variables, but their efficiencies are directly measured on selected samples of data, which are used also to study the properties of the remaining backgrounds.

Specific procedures have been designed for the $\gamma\gamma$ and cosmic ray background rejection. They are described in detail in the following.

To cross-check the photon identification and reconstruction, an inclusive one-prong hadronic analysis, which infers the polarisation from the charged pion momentum distribution, has been devised, in addition to the standard study of the previously listed channels.

4.2 Tools

The general tools applied in the analysis are presented here. Additional information on their performances is given in Sect. 4.4 dedicated to the study of the systematic uncertainties.

4.2.1 Charged particle identification

The charged particle identification procedure (PID) described in [11] is used for the non-τ background rejection and for the decay channel selection.

Charged particles are classified as electron, muon, or hadron (pions and kaons are treated as a single class thereafter referred to as "pions"). Since there is negligible probability of mistaking electron and muon ($\sim 2.5{\times}10^{-4}$), the PID is based on two likelihood estimators which give the relative probability for a track to be an electron versus a pion (e/π), and to be a muon versus a pion (μ/π), respectively. The μ/π PID is restricted to charged tracks with momentum above 1.3 GeV/c. An identification efficiency of about 99% with a rate of misidentification of about 1% is achieved for the μ's in the previously defined region and for the electrons inside a fiducial region which excludes about twice the size of the physical ECAL cracks. A study of selected data samples [11] has shown that the efficiencies are reproduced by the Monte Carlo at the two per mil level. The small resultant corrections are applied in the polarisation measurements.

4.2.2 Photon reconstruction

The reconstruction of photons from clusters of cells in the electromagnetic calorimeter is performed with the ALEPH standard algorithm [10] which searches for local energy maxima in the ECAL pad clusters. Fluctuations of a shower can generate "fake photons" [17] which are artefacts of the clustering algorithm or true photons produced by secondary interactions in the ECAL.

In order to reduce the number of such fake photons, an estimator of fakeness (P_{fak}) is built from the relevant parameters [17]: the oriented distance to the closest charged track, the fraction of the shower energy deposited in the first ECAL stack, and the total ECAL shower energy. The sign of the distance is computed depending of the position of the shower with respect to the track bending in the $r-\phi$ projection.

The reference distributions are taken from Monte Carlo, with the ECAL barrel and end-cap being handled independently. A cut on the fakeness likelihood estimator provides a partition of the photon candidate sample in two subsamples: the "fake photon" sample (P_{fak} >0.75), enriched in fake photons and the "genuine photon" sample (P_{fak} <0.75), enriched in genuine photons. The distributions of the variables used to construct the P_{fak} estimator are shown in Fig. 1 for each of the two subsamples of photon candidates. A good agreement between data and $\tau^+\tau^-$ Monte Carlo can be observed.

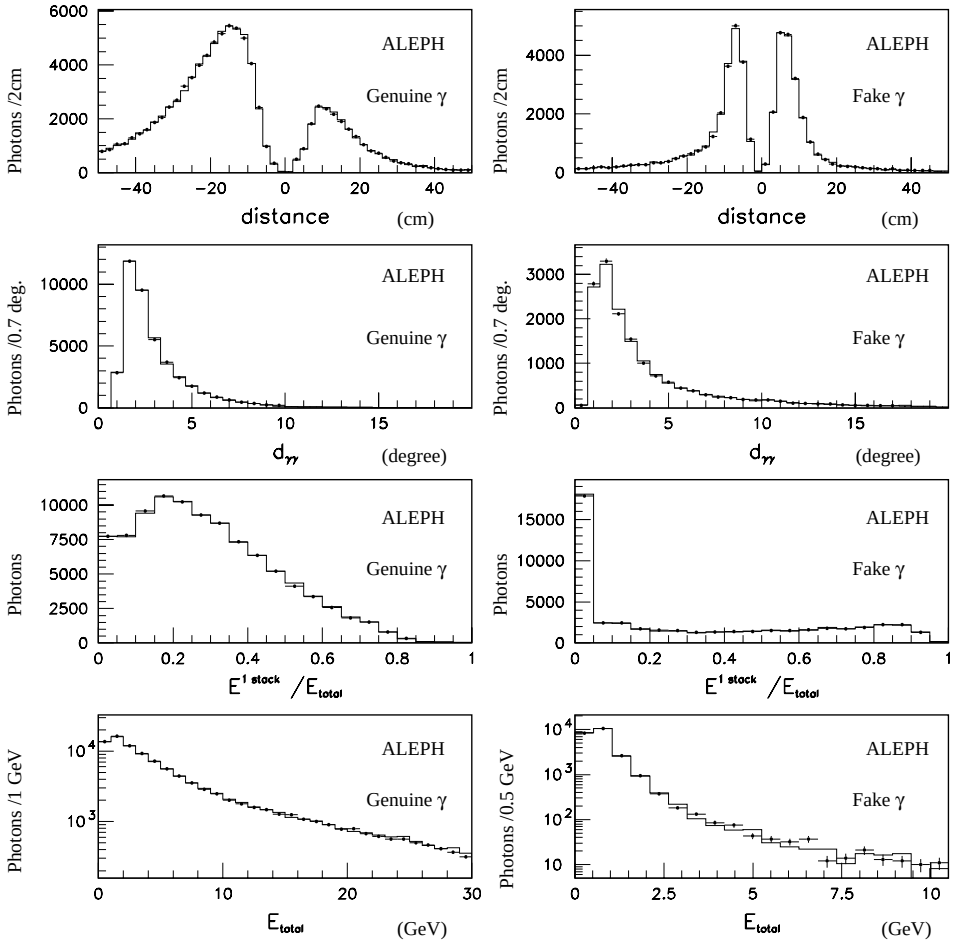

Fig. 1. Distributions of the variables used to define estimators for genuine and fake photons. Data are represented by points while the histograms are the predictions of the simulation. Discriminant variables are described in the text. In each plot the distributions for data and Monte Carlo are normalized to the same number of photons. The distance $d_{\gamma\gamma}$ [17] is used in the second analysis only

4.2.3 Non-τ background rejection

Non-τ background in the selected samples has four main sources: Bhabha events, $Z \to \mu^+\mu^-$ decays, $Z \to q\bar{q}$ decays, and $\gamma\gamma$ processes. As stated before, likelihood estimators exploiting the information of a single hemisphere are used for the suppression of the backgrounds that arise from the first three categories.

The Bhabha estimator ($\mathcal{E}^{e^+e^-}$) provides the likelihood for one hemisphere to be part of a Bhabha event rather than of a $\tau^+\tau^-$. It is based on three variables: the e/π probability of the track, its momentum, and the ECAL wire energy. Specific reference distributions are used for tracks pointing to an ECAL crack.

The $Z \to \mu^+\mu^-$ estimator ($\mathcal{E}^{\mu^+\mu^-}$) is similar to the previous one with the μ/π track probability replacing the e/π probability.

A third estimator ($\mathcal{E}^{q\bar{q}}$) tags a Z hadronic decay in one hemisphere. It makes use of the opening angle between the charged tracks, the number of charged tracks, the number of objects reconstructed from the pattern of the energy deposited in the calorimeters, and the mass and energy of the jet. It is very similar to the estimator used for the leptonic cross section measurement and is described in [11] and [18]. Different reference distributions are taken for each ECAL region (barrel, endcaps, and their overlap).

The $\gamma\gamma$ background is rejected by cuts on the three pertinent variables: visible energy, missing transverse momentum, and acollinearity of the two jets. The cut values are optimized for each final state.

Two less important backgrounds can also contribute: $\ell^+\ell^-$V and cosmic ray events. The $\ell^+\ell^-$V events are eliminated by the same cuts that reject Bhabha, $Z \to \mu^+\mu^-$, and $Z \to q\bar{q}$ events.

Cosmic rays can contaminate the $\tau \to h\nu$ and $\tau \to \mu\nu\bar{\nu}$ channels. They appear as events with two collinear tracks of the same momentum coming from the vertex region and a low energy deposit in the electromagnetic calorimeter. A first set of cuts is applied to select them: ECAL energy below 2.5 GeV, $|p_1| - |p_2| < 5.0\,\mathrm{GeV}/c$, $\min(|d_0^1|, |d_0^2|) > 0.1\,\mathrm{cm}$, and $|d_0^1 + d_0^2| < 0.5\,\mathrm{cm}$, where p_i and d_0^i are respectively the momentum and signed impact parameter of the track i. The short gating time of the ITC is then used [19]. On the sample of cosmic ray candidates selected by the preceding cuts, the distribution of the number of ITC hits is measured. It is found that 68% of the events have no hits and 88% less than eight. Since the number of ITC hits is related only to the arrival time of the particles, the comparison of its distributions in the two samples, cosmic ray candidates and τ decays, is used first to estimate quantitatively the residual background in the τ samples. Finally, the events in the previously defined sample are

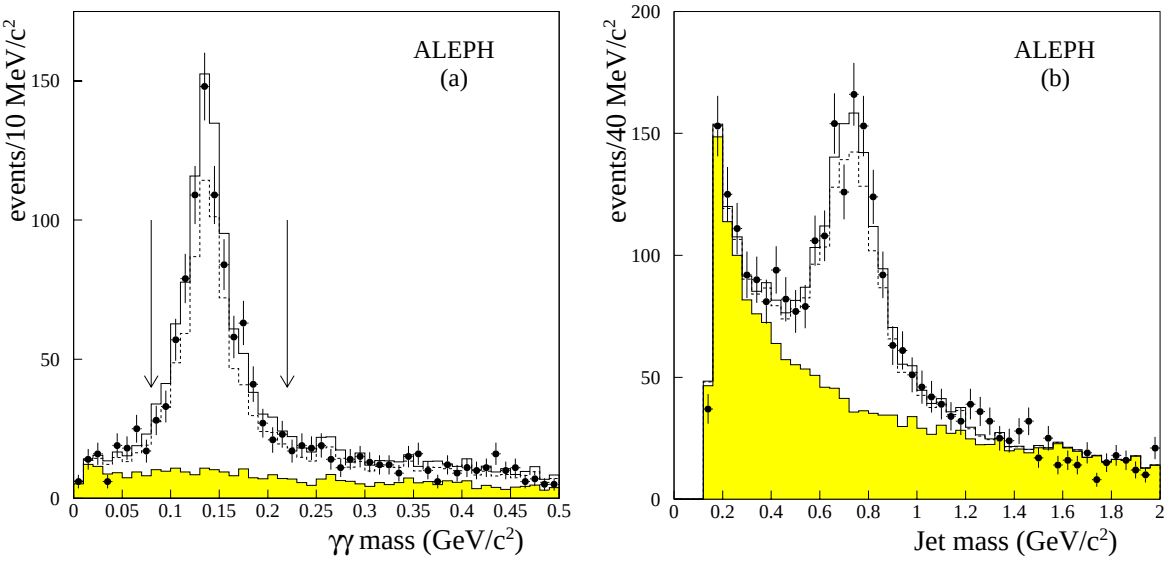

Fig. 2. a The $\gamma\gamma$ mass distribution for the "electron" hemispheres with a jet mass larger than 0.5 GeV/c^2. The shaded area is the contribution of $\tau \to e\nu\bar{\nu}$ taken from the $\tau^+\tau^-$ Monte Carlo. **b** The "$\pi^{\pm}$"(γ(s)) mass distribution in the muon sample before the hadronic veto. The shaded area shows the contribution of $\tau \to \mu\nu\bar{\nu}$ taken from the $\tau^+\tau^-$ Monte Carlo. The black dots are the data, the solid (dashed) histogram the $\tau^+\tau^-$ Monte Carlo prediction taking (not taking) into account the correction to the hadron misidentification rate described in Sect. 4.2.1

rejected, along with events satisfying the same criteria on ECAL energy and momenta, and $N_{ITC} < 8$.

4.3 Channel selection

The ALEPH standard leptonic pre-selection described in [11], which essentially requires a multiplicity of charged tracks between two and eight, is used first. The different channels are then selected in the angular acceptance ($|\cos\theta| < 0.9$) with the help of the charged particle and photon identification.

4.3.1 Leptonic decays

The leptonic τ decay sample is selected from hemispheres containing only one charged track coming from the interaction region and identified as electron or μ. In the case of electron, it is required that the charged track does not point to an ECAL crack. To reduce the hadronic τ decay background possibly arising from particle misidentification, it is required that there is no genuine γ pair with an invariant mass compatible with the π^0 mass, and that the jet (hemisphere) mass is smaller than 0.5 GeV/c^2. Since bremsstrahlung is only significant for electrons, muon hemispheres with one or more photons are also rejected when the hemisphere mass lies between 0.5 GeV/c^2 and 1.6 GeV/c^2. This "hadronic veto" is illustrated by Fig. 2 which shows the $\gamma\gamma$ mass in electron hemispheres, and the jet mass in muon hemispheres containing at least one photon.

The non-τ background is rejected by cuts on the above described $\mathcal{E}^{e^+e^-}$ and $\mathcal{E}^{\mu^+\mu^-}$ estimators. To further suppress the Bhabha event contamination in the electron channel, the total ECAL wire energy is required to be smaller than 0.9 $\sqrt{s}$. The ECAL wire energy distribution, before this last cut, is shown in Fig. 3. The agreement observed between the data and the sum of signal and background Monte Carlo shows the good understanding of the non-τ background contamination in the electron channel.

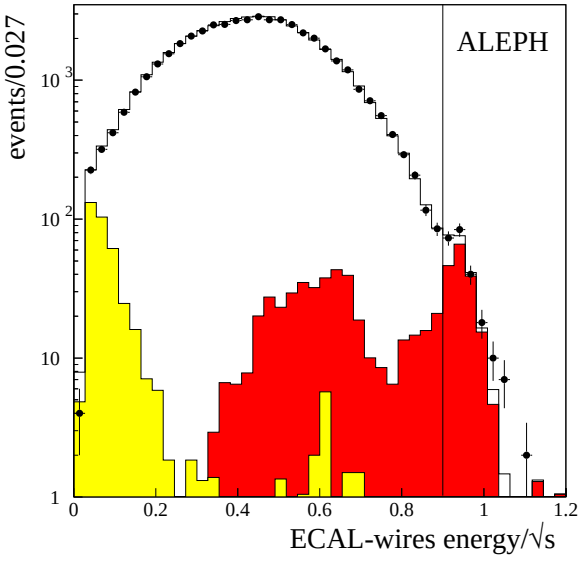

Fig. 3. Distribution of the total ECAL wire energy, normalized to the centre-of-mass energy, in the electron channel. The black dots represent the data, the line histogram the sum of all contributions, $\tau^+\tau^-$, $\gamma\gamma \to e^+e^-$, $\gamma\gamma \to \tau^+\tau^-$, and Bhabha events, given by Monte Carlo. Grey histograms, represent the backgrounds: dark grey for Bhabha events and light grey for $\gamma\gamma$ interactions. The vertical line displays the cut value

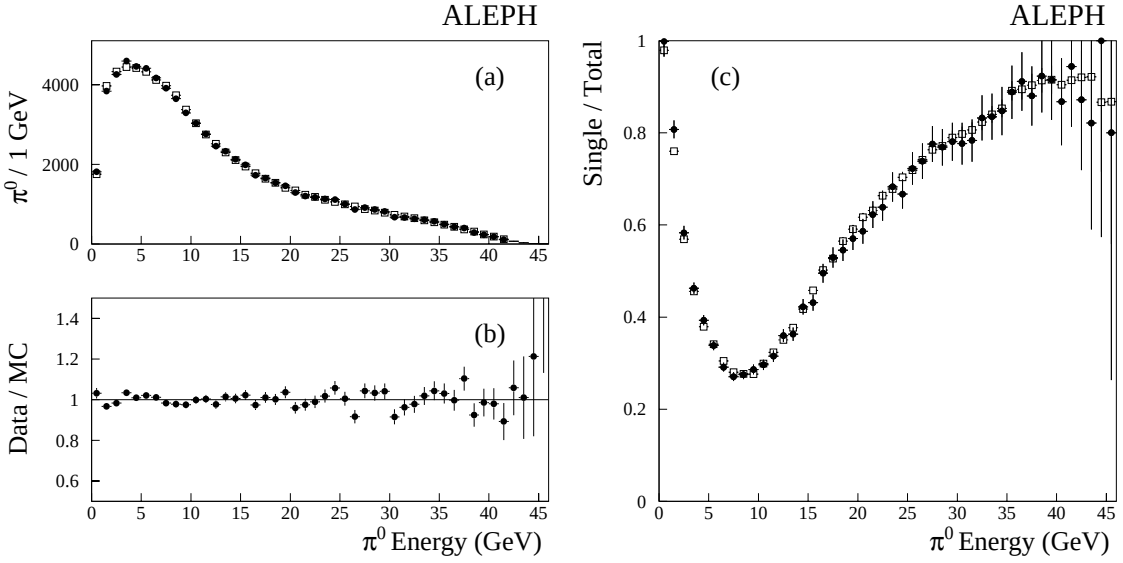

Fig. 4. a Distribution of the π^0 energy data (black dots) and $\tau^+\tau^-$ Monte Carlo (empty squares). **b** Data over Monte Carlo ratio. **c** Single photon fraction in the π^0 sample as a function of the π^0 energy

The two-photon background is rejected by the cuts defined in the previous section.

4.3.2 $\tau \to h\nu$

For the selection of hadronic decays without a neutral hadron, the presence of only one charged track coming from the vertex region, with a momentum larger than 1.3 GeV/c (limit of the validity of μ-PID), is required. It is also required that this track is not identified as an electron or a muon by the PID. Two further cuts are imposed on the same hemisphere: no genuine reconstructed photon and a calorimetric energy deposit consistent with the momentum of the charged hadron. This last cut reduces the $K^0_L\pi$ background.

The rejection of the hadronic Z decays and other non-τ backgrounds is performed by cuts on the values of the previously defined likelihood estimators computed on the opposite hemisphere. The two-photon background is rejected by the cuts described in Sect. 4.2.3.

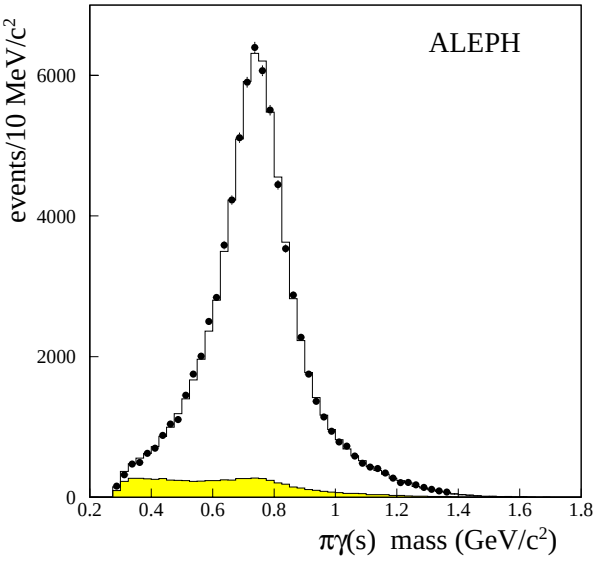

Fig. 5. Distribution of the $\pi^{\pm}\gamma$(s) mass for data (black dots) and $\tau^+\tau^-$ Monte Carlo (histogram), in the $\tau \to \rho\nu$ sample. The shaded histogram shows the contribution of τ background

4.3.3 $\tau \to \rho\nu$

This selection is similar to the $h\nu$ channel selection as far as the characteristics of the charged track and the non-τ background rejection are concerned. The requirements on the photons in the charged track hemisphere are opposite. The presence of one or two genuine photons is required. When a single photon is reconstructed, its energy must be greater than 0.5 GeV and a cut on the $\pi\gamma$ mass ($0.4\,\mathrm{GeV}/c^2 < m_{\pi\gamma} < 1.6\,\mathrm{GeV}/c^2$) is imposed. When two photons are reconstructed, no cut on the $\pi 2\gamma$ mass is applied but the $\gamma\gamma$ mass has to be compatible with a π^0 mass ($80\,\mathrm{MeV}/c^2 < m_{\gamma\gamma} < 250\,\mathrm{MeV}/c^2$).

The quality of the simulation is illustrated in Fig. 4, which shows the π^0 (one and two γ(s)) energy distribution in the selected ρ sample along with the single photon fraction, and in Fig. 5, where the jet mass in the one γ sample (before the above described cut on this mass) is displayed.

4.3.4 $\tau \to a_1\nu$, $a_1 \to h2\pi^0$

Here also, the selection criteria on the charged track and the non-τ background rejection are the same as in the $h\nu$

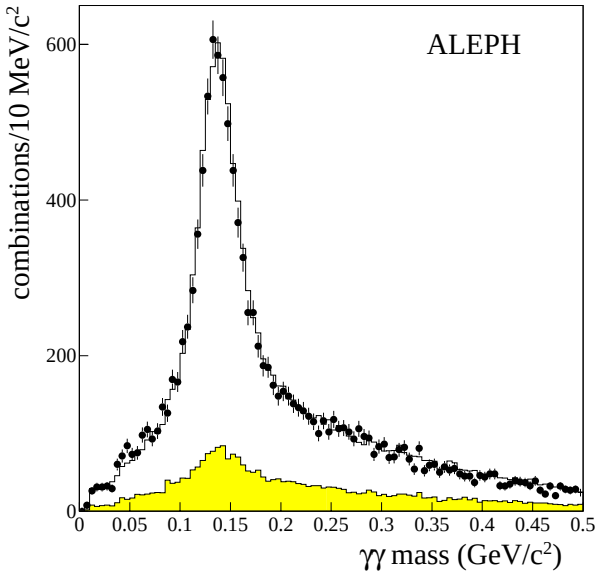

Fig. 6. Distribution of the $\gamma\gamma$ mass in four photon hemispheres when the effective mass of the two other photons is in the π^0 region. Data are represented by black dots and Monte Carlo by histograms. The shaded histogram shows the contribution of τ background

case. The additional requirements on the photons in the selected hemisphere are as follows. The number of genuine reconstructed photons, n_γ, ranges from two to four. For $n_\gamma = 2$, the $\gamma\gamma$ mass has to be larger than the π^0 mass and inconsistent with it. For $n_\gamma = 3$, the reconstruction of at least one π^0 is required and, for $n_\gamma = 4$, the reconstruction of two π^0's is required. The choice of the best association of the photons and the π^0 reconstruction are performed by a kinematic fit [10] which also improves the energy determination.

The purity of the selection and the quality of the reconstruction for the four photon sample are shown in Fig. 6 where the mass of a $\gamma\gamma$ system is displayed when the mass of the two remaining photons is consistent with the π^0 hypothesis.

4.3.5 $\tau \to a_1\nu$, $a_1 \to 3h$

The presence of three charged tracks coming from the interaction region is required. At least two of the three tracks must be identified as charged hadrons by the PID. The following cuts against the presence of π^0's in the hemisphere are applied: no genuine photon with energy larger than 1 GeV, no genuine γ pair with $E_{\gamma\gamma} > 3\,\mathrm{GeV}$, and $m_{\gamma\gamma}$ compatible with m_{π^0}. Hemispheres containing a V^0, as defined by the ALEPH V^0 package [10], whose mass is compatible with a K^0_S are rejected. In addition, the effective mass of at least one of the $\pi^-\pi^+$ combinations is required to be larger than $0.55\,\mathrm{GeV}/c^2$. The non-τ background rejection is the same as in the other hadronic decay channels.

Table 2. Summary of the systematic uncertainties (%) on A_τ and A_e in the single-τ analysis

	A_τ						
Source	h	ρ	$3\,h$	$h\,2\pi^0$	e	μ	Incl. h
selection	-	0.01	-	-	0.14	0.02	0.08
tracking	0.06	-	0.22	-	-	0.10	-
ECAL scale	0.15	0.11	0.21	1.10	0.47	-	-
PID	0.15	0.06	0.04	0.01	0.07	0.07	0.18
misid.	0.05	-	-	-	0.08	0.03	0.05
photon	0.22	0.24	0.37	0.22	-	-	-
non-τ back.	0.19	0.08	0.05	0.18	0.54	0.67	0.15
τ BR	0.09	0.04	0.10	0.26	0.03	0.03	0.78
modelling	-	-	0.70	0.70	-	-	0.09
MC stat	0.30	0.26	0.49	0.63	0.61	0.63	0.26
TOTAL	0.49	0.38	1.00	1.52	0.96	0.93	0.87
	A_e						
Source	h	ρ	$3\,h$	$h\,2\pi^0$	e	μ	Incl. h
tracking	0.04	-	-	-	-	0.05	-
non-τ back.	0.11	0.09	0.04	0.22	0.91	0.24	0.17
modelling	-	-	0.40	0.40	-	-	-
TOTAL	0.12	0.09	0.40	0.47	0.91	0.25	0.17

4.3.6 Inclusive channel $\tau \to h \geq 0\gamma\nu$

The charged track selection and the non-τ background rejection are those used in the selection of the $h\nu$ channel. Only the cuts against the two-photon event background are tighter, because the pion momentum distribution used for the polarisation measurement is very sensitive to this background. Since the purpose of the study of the inclusive channel is to cross-check the photon and π^0 treatment, no cut using information from the electromagnetic calorimeter in the selected hemisphere is applied.

4.4 Systematic uncertainties

The sources of systematic errors affecting the τ polarisation measurement are:

- τ selection efficiency,
- non-τ background contamination,
- γ/π^0 reconstruction,
- energy/momentum calibration,
- modelling of a_1 decay and radiative processes,
- τ decay channel cross-talk.

A summary of the errors in the single-τ method is given in Table 2 and their estimation is discussed in the following.

The dominant contributions are photon/π^0 reconstruction, ECAL calibration, non-τ background, and modelling of the decay for the a_1. This last effect is evaluated [2] by changing the model and its parameters within the limits allowed by the data.

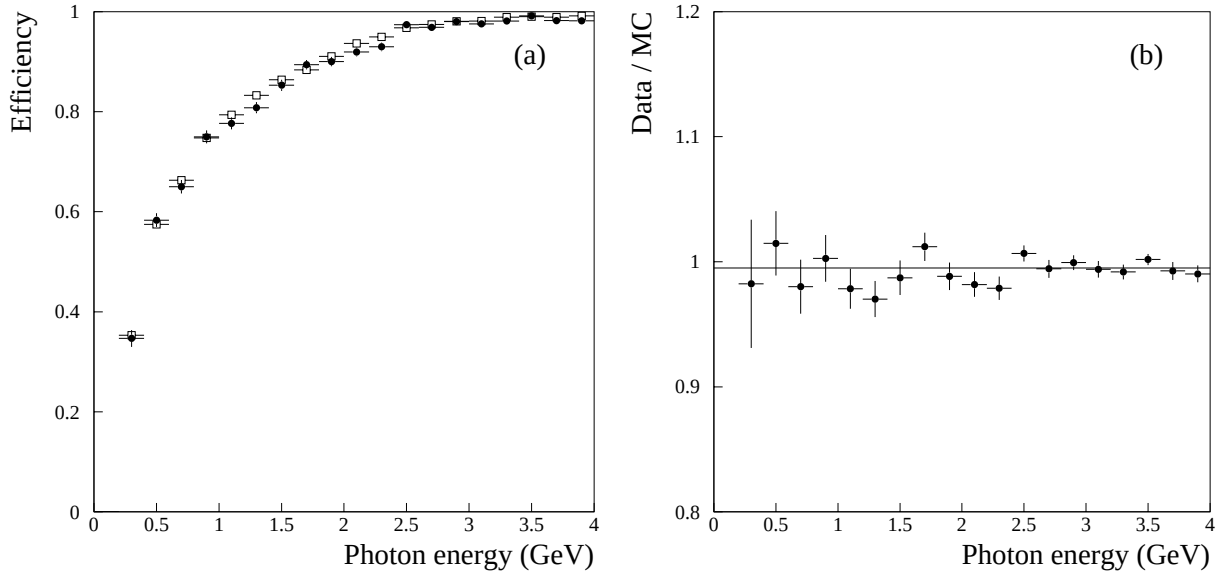

Fig. 7. **a** Efficiency of the fake photon estimator for genuine photons. The black dots are the data, the empty squares the $\tau^+\tau^-$ Monte Carlo. **b** Data/Monte Carlo ratio for this efficiency

The systematic effects are evaluated for each of the previously described tools using the difference between the data and Monte Carlo plus one standard deviation as input. The errors are propagated through all the steps of the analysis, taking into account the fact that a given tool can be used in several places. For that, A_τ and A_e are measured by means of the standard $\hat{W}^{\pm}(\omega)$ functions on Monte Carlo events weighted for the change of the tool response. The shifts of the values of A_τ and A_e give the associated errors. Cross-checks of the estimations are presented for some of the important contributions.

4.4.1 Charged particle identification

The comparison of the PID performances on data and Monte Carlo is reported in [11]. The uncertainty on the data/Monte Carlo efficiency-ratio computed for each year of data taking is used to estimate systematic error.

4.4.2 Photon reconstruction

Clustering algorithm. The first step of photon reconstruction is the "standard" ALEPH clustering algorithm [10]. Its parameters are the distance to the closest charged track and the threshold energy. It has been shown in [17] that the distance parameter can be changed by 1 mm, while preserving within one standard deviation the agreement between data and Monte Carlo on the distance distribution. This parameter shift introduced in the simulation induces negligible effects on the polarisation, even in channels containing photon(s). The possible effect of the threshold value is investigated by modifying the reconstructed shower energy in the Monte Carlo by the clustering correction [10]. The resulting variation of the polarisation measurement is small but not completely negligible. It is part of the value given in the line "photon" of Table 2.

Fake photon estimator. The second step is the genuine/fake classification for which the P_{fak} estimator is used. In the first place, the efficiency of the identification of genuine photons is measured on a selected sample made of photons forming a π^0 with one "high quality"photon (converted γ or isolated shower with $4\,\mathrm{GeV} < E < 20\,\mathrm{GeV}$). For energies greater than 4 GeV, the efficiency is not significantly different from one. The efficiencies for $E < 4\,\mathrm{GeV}$ are shown in Fig. 7. The ratio between data and Monte Carlo is $(99.50\pm0.19)\times10^{-2}$ and an efficiency variation of 0.69×10^{-2} is used as input in the error computation.

Since the Monte Carlo is able to reproduce the characteristics of the fake photon production in a hadronic shower but not its precise normalization [17], a weighting procedure is used to correct it. The weight for an event is written $w(p)^n$, where n is the fake photon multiplicity and p the hadron momentum. The function $w(p)$ is obtained by a fit of the likelihood estimator distributions. A check of the procedure is given by the comparison of data and Monte Carlo for the $\gamma\gamma$ mass spectra shown in Fig. 8. The related systematic error is estimated in the standard way described at the beginning of Sect. 4.4, comparing the measured weight to one.

4.4.3 Bhabha, $\mu^+\mu^-$, and $q\bar{q}$ event backgrounds

Efficiency of the estimators. The $\mathcal{E}^{e^+e^-}$, $\mathcal{E}^{\mu^+\mu^-}$, and $\mathcal{E}^{q\bar{q}}$ estimators use information from only one of the hemispheres of an event, so correlations with the other hemisphere can only be due to geometrical correlations in the detector construction (ECAL cracks, overlap, etc.). The

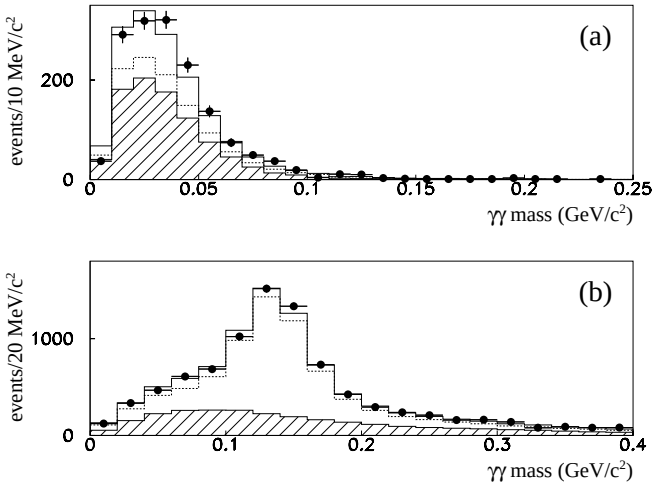

Fig. 8a,b. The $\gamma\gamma$ mass spectrum, for a sample of $\pi\gamma\gamma$ hemispheres: **a** when the two photons are classified as fake, **b** when 1 photon is classified as fake and the other as genuine. The black dots are the data, the dashed line histogram the $\tau^+\tau^-$ Monte Carlo and the full line histogram the $\tau^+\tau^-$ Monte Carlo, with a weighted fake photon contribution. The hatched histogram is the fake photon contribution in the $\tau^+\tau^-$ Monte Carlo, without weighting (see text)

Table 3. Efficiencies of the $\mathcal{E}^{e^+e^-}$ and $\mathcal{E}^{\mu^+\mu^-}$ estimators (in %) measured on data and Monte Carlo samples

	$\mathcal{E}^{e^+e^-}$	
	DATA	M.C.
$\tau^+\tau^-$	98.92 ± 0.03	98.95 ± 0.01
e^+e^-	2.77 ± 0.02	2.66 ± 0.02
	$\mathcal{E}^{\mu^+\mu^-}$	
	DATA	M.C.
$\tau^+\tau^-$	99.45 ± 0.03	99.48 ± 0.01
$\mu^+\mu^-$	0.17 ± 0.04	0.16 ± 0.05

measurement of the estimator efficiencies in the non-correlated regions is described first, and then an evaluation of the residual background, which is not affected by the possible correlations, is presented. This last point concerns only the hadronic channels because the selection criteria for leptonic τ decays eliminate the correlated, insensitive parts of the detector.

In order to measure the efficiencies, almost pure samples of data and Monte Carlo events are selected for the $\tau^+\tau^-$, e^+e^-, $\mu^+\mu^-$, and $q\bar{q}$ final states. A clean τ decay (three charged π's or a ρ), a high energy electron, a high energy muon or a hadronic jet is required in one hemisphere and the opposite one is used to study the estimators. Examples of their responses in the case of $\mathcal{E}^{e^+e^-}$ and $\mathcal{E}^{\mu^+\mu^-}$ are shown in Fig. 9 and 10.

A cut at a value of 0.8 on these two estimators allows a good separation between τ's and leptonic background. The measured efficiencies, taking into account the small residual contamination of the samples, are given in Table 3. These numbers are used to determine the systematic uncertainties which contribute to the line "selection" of Table 2 and to the line "non-τ background" for the two leptonic channels.

A similar analysis, already described in [11], is performed for the $\mathcal{E}^{q\bar{q}}$ estimator.

Residual backgrounds. The estimation of the residual background, chiefly Bhabha events, in the hadronic channels is an essential task on account of its impact on the $\mathcal{A}_e$ measurement. For that reason, procedures were developed to measure directly the background contributions from the data themselves.

The method is exemplified by the case of the $\tau \to h\nu$ channel. Applying all the cuts used for the channel selection but the e/π identification cut on the τ side, and the $\mathcal{E}^{e^+e^-}$ cut on the opposite one, a set of data is constituted which is divided in two subsets by the response of the e/π PID: (a) for e PID and (b) for π PID. The distributions of $\mathcal{E}^{e^+e^-}$ in the two subsets and the $\tau^+\tau^-$ Monte Carlo expectations shown in Fig. 11 clearly display the Bhabha event background.

The events with $\mathcal{E}^{e^+e^-} > 0.8$ in sample (b) are used to determine the kinematic characteristics of this background. The normalization of the residual background after the $\mathcal{E}^{e^+e^-}$ cut is given by the number of events with $\mathcal{E}^{e^+e^-} > 0.8$ in sample (b) multiplied by the ratio of the numbers of events with $\mathcal{E}^{e^+e^-} < 0.8$ and $\mathcal{E}^{e^+e^-} > 0.8$ in sample (a). This background is subtracted for the polarisation measurement and the statistical error on its estimation enters the systematic error. The small difference of the efficiencies of the cut on $\mathcal{E}^{e^+e^-}$ in samples (a) and (b), mainly due to geometrical effects and initial state radiation, can be computed by Monte Carlo and is added to the systematic uncertainty.

As a cross-check, an independent study of the Bhabha event background has been performed, using the tools developed for the measurement of the τ leptonic branching ratios [19]. Its conclusions are consistent with the above presented results.

Similar procedures are used to study the $\mu^+\mu^-$ contamination. They show that such a background is reduced to a negligible level by the selection process.

4.4.4 Other backgrounds

Two-photon background. In a similar way, the residual $\gamma\gamma$ background can be studied in the data from the excesses of events in the distributions of the variables (acollinearity, visible energy, etc.) used for its rejection.

$\ell^+\ell^-$V *background.* Such a background appears mostly in the leptonic channels. The contaminations evaluated by a study of the opposite hemispheres are $(0.2 \pm 3.2) \times 10^{-4}$ for the electron channel and $(5.5 \pm 3.6) \times 10^{-4}$ for the

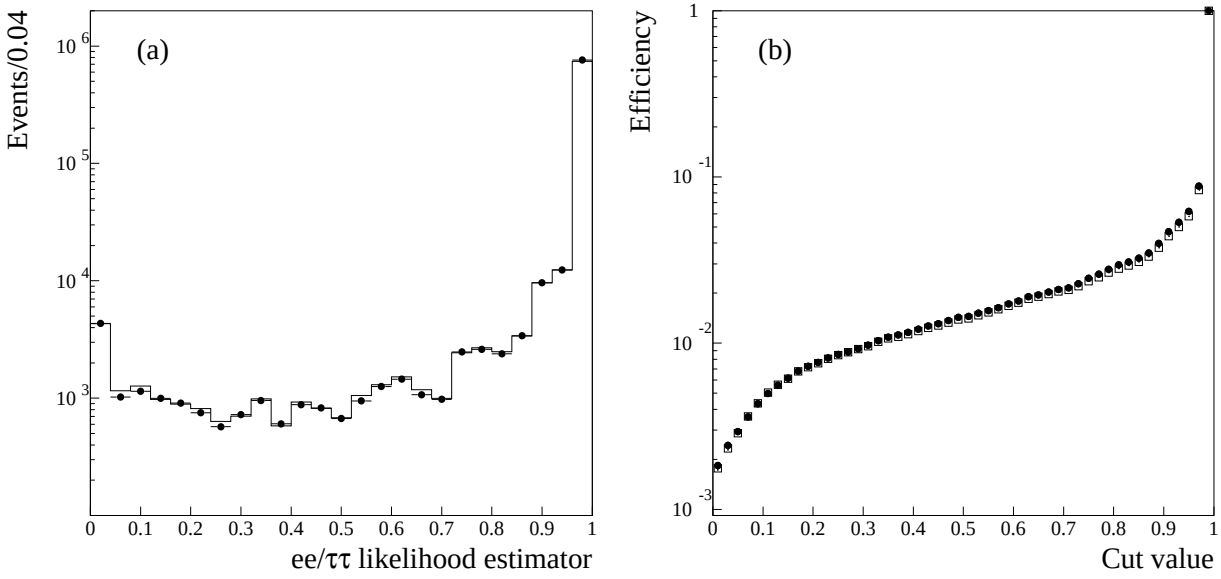

Fig. 9. a The $\mathcal{E}^{e^+e^-}$ distribution after tagging an electron in the opposite hemisphere. **b** Efficiency on Bhabha events as function of the cut value. Black dots are the data, empty boxes and histogram, the Bhabha Monte Carlo

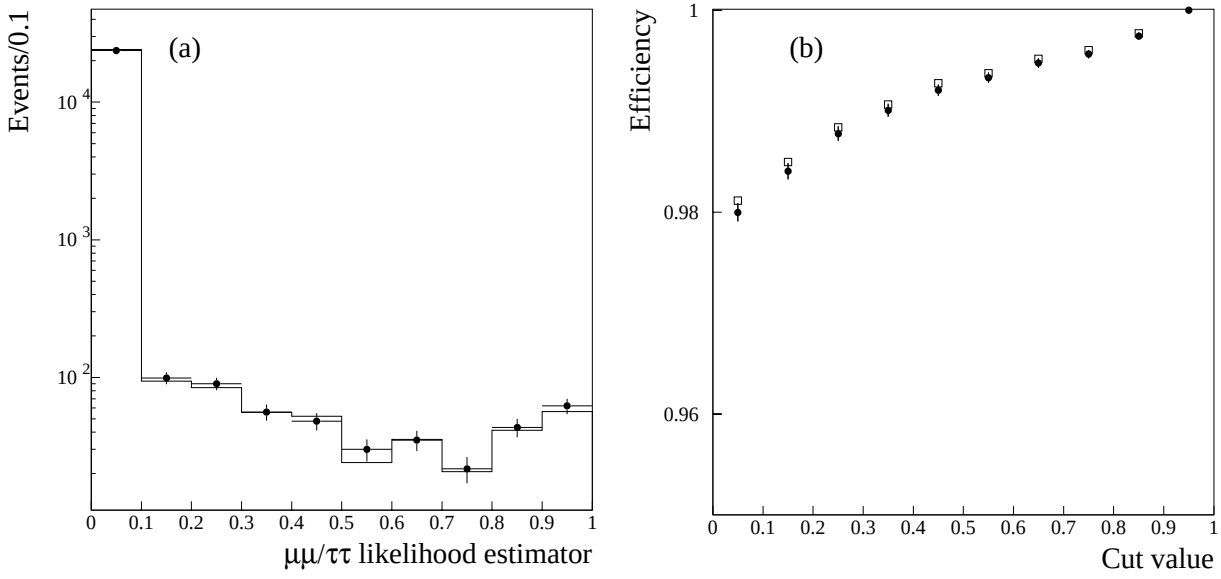

Fig. 10. a The $\mathcal{E}^{\mu^+\mu^-}$ distribution after tagging a τ in the opposite hemisphere. **b** Efficiency on $\tau^+\tau^-$ events as function of the cut value. Black dots are the data, empty boxes and histogram, the $\tau^+\tau^-$ Monte Carlo

muon. To compute the tiny associated uncertainties the FERMISV Monte Carlo [16] is used.

Cosmic ray background. The contaminations of the two relevant channels, $\tau \to h\nu$ and $\tau \to \mu\nu\bar{\nu}$ are estimated using the independent information from the track parameters and the number of ITC hits. Their values are $(6.9 \pm 1.9) \times 10^{-4}$ and $(1.5 \pm 0.5) \times 10^{-4}$ respectively, leading to very small contributions to the uncertainties. Out-of-time cosmic rays are normally identified as hadrons, owing to the HCAL and muon chamber inefficiency in such events [19].

τ background. Uncertainties due to the crosstalk between different decay channels are evaluated by varying within their errors the different branching ratios used in the Monte Carlo.

4.4.5 Detector calibration

Momentum calibration. The uncertainty on the momentum calibration described in Sect. 3.1 is used, for each $\cos\theta$ bin, to estimate the contribution to the polarisation systematic errors.

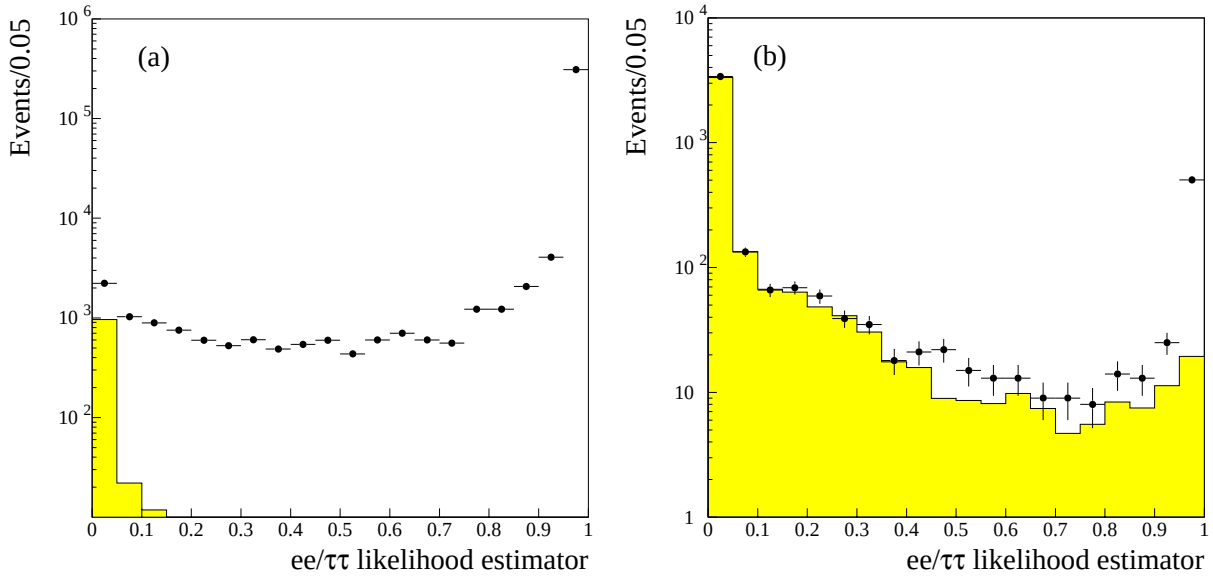

Fig. 11a,b. The distribution of the $\mathcal{E}^{e^+e^-}$ estimator in the $h\nu$ channel, **a** for events with an electron identification, **b** for a pion identification. The shaded histograms are the $\tau^+\tau^-$ Monte Carlo predictions

ECAL calibration. The ECAL energy calibration (Sect. 3.1) is obtained from electrons taken in Bhabha events, $\gamma\gamma$ processes, or τ decays to electrons. Uncertainties coming from the statistics of these samples and the handling of the ECAL saturation are introduced as systematic errors, leading to an uncertainty of $2.5\times\ 10^{-3}$ on the calibration, which is used as input for the computation of polarisation errors.

An independent check of the ECAL calibration has been performed using the $\mu^+\mu^-\gamma$ events for which the photon energy is deduced, with a small error, from the angles, by the formula

$$E_\gamma^{\text{calc.}} = \frac{\sin\theta_{\mu^+\mu^-}\sqrt{s}}{\sin\theta_{\mu^+\mu^-} + \sin\theta_{\mu^+\gamma} + \sin\theta_{\gamma\mu^-}} \ .$$

The distributions of $\Delta E_\gamma/\sigma_{E_\gamma}$, where ΔE_γ is the difference $E_\gamma^{\text{calc.}} - E_\gamma^{\text{rec.}}$ between the kinematically calculated and ECAL energies, and σ_{E_γ} the expected resolution, are shown in Fig. 12 for data and Monte Carlo and a very good agreement can be observed.

Since some calorimetric cuts are used in the selection of the two hadronic final states without photons, a tuning of the ECAL response to charged hadrons is also performed. The related uncertainties are independently evaluated.

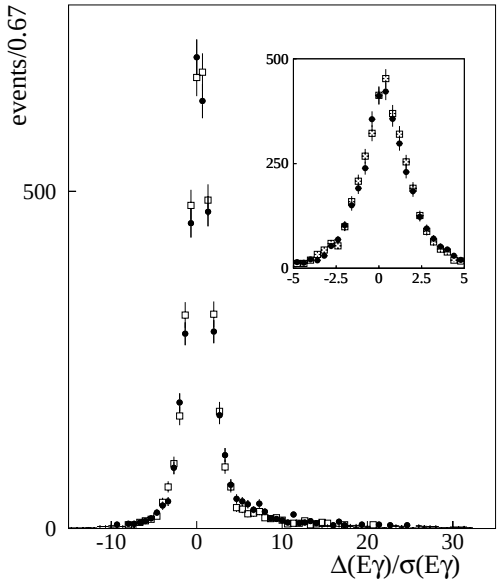

Fig. 12. Difference between the reconstructed and calculated photon energy, $\Delta E\gamma/\sigma_{E\gamma}$ for $\mu^+\mu^-\gamma$ events. The insert is a zoom of the region [-5,5]. The black dots represent the data and the empty squares the $\mu^+\mu^-\gamma$ Monte Carlo

4.5 Results

Table 4 gives the numbers of selected data events, the selection efficiencies in the angular acceptance, and the contaminations from τ and non-τ backgrounds.

The polarisation is measured independently for each channel and for each year of data taking. Some of the systematic errors are common to all the years and some are common to different channels.

In a first step, the measurements for each channel in the different LEP operation periods are combined, taking care of the common systematic errors and adding the small corrections dependent on the centre-of-mass energy described in Sect. 6.1. The values obtained are given in the corresponding lines of Table 5.

Figure 13 shows the x distributions for the hadron, muon, and electron channels; and the ω distributions for the $\rho\nu$ and $a_1\nu$ channels ($3h$ and $h2\pi^0$). The distributions for data and the contributions (Monte Carlo) from the two τ helicities and non-τ background are superimposed.

Table 4. Number of selected events in the data, selection efficiency within the angular acceptance, and contamination from the τ background and the non-τ background. In the $3h$ mode, the $KK\pi$ and $K\pi\pi$ modes are treated as τ background

Channel	h	ρ	$3h$	$h2\pi^0$	$3h$	$h2\pi^0$	Incl.h
candidates	34249	75296	27854	27924	47106	50585	134108
efficiency (%)	76.6	78.1	77.2	66.9	75.9	86.4	63.3
τ back. (%)	10.6	10.9	10.9	24.3	0.8	0.7	0.5
Bhabha back. (%)	0.16 ± 0.03	0.07 ± 0.02	0.06 ± 0.05	0.10 ± 0.08	1.00 ± 0.03	-	0.07 ± 0.01
other non-τ back. (%)	0.24	0.11	0.11	0.09	0.50	0.30	0.40

Table 5. Results for $\mathcal{A}_\tau$ and $\mathcal{A}_e$ obtained with the single-τ analysis. The first error is statistical, the second systematic

Channel	$\mathcal{A}_\tau$ (%)	$\mathcal{A}_e$ (%)
hadron	$15.21 \pm 0.98 \pm 0.49$	$15.28 \pm 1.30 \pm 0.12$
rho	$13.79 \pm 0.84 \pm 0.38$	$14.66 \pm 1.12 \pm 0.09$
a1(3h)	$14.77 \pm 1.60 \pm 1.00$	$13.58 \pm 2.11 \pm 0.40$
a1(h2π^0)	$16.34 \pm 2.06 \pm 1.52$	$15.62 \pm 2.72 \pm 0.47$
electron	$13.64 \pm 2.33 \pm 0.96$	$14.09 \pm 3.17 \pm 0.91$
muon	$13.64 \pm 2.09 \pm 0.93$	$11.77 \pm 2.77 \pm 0.25$
pion inclusive	$14.93 \pm 0.83 \pm 0.87$	$14.91 \pm 1.11 \pm 0.17$
Combined	$14.44 \pm 0.55 \pm 0.27$	$14.58 \pm 0.73 \pm 0.10$

The measurements from all the channels are then combined taking into account their correlations evaluated by Monte Carlo. The inclusive hadronic analysis has been devised as a cross-check of the exclusive ones since their systematic uncertainties are essentially uncorrelated. The values given in Table 5 show that this test is satisfactory. Statistically, on the contrary, the exclusive and inclusive analyses are strongly correlated so that the inclusive measurement brings only little new information in the final result.

The final values of $\mathcal{A}_e$ and $\mathcal{A}_\tau$ are given in the last line of Table 5. Their errors are corrected for the correlation between opposite hemispheres.

As an illustration of the understanding of the ρ channel, Fig. 14 shows the τ and ρ decay angle distributions with good agreement between data and Monte Carlo, even for low energy ρ's ($\cos\psi_\tau < -0.9$).

5 Analysis with the τ direction method

5.1 Philosophy of the method

The τ polarisation analysis described in this section is based on two ideas: use of proven analysis tools and enhancement of the measurement sensitivity. On one hand, event selection, particle identification, photon and π^0 reconstruction, and decay classification are taken from previous ALEPH analyses of τ leptonic and hadronic branching ratios [17,19], and of the hadronic spectral functions [20,21]. On the other hand, the maximum sensitivity to the τ polarisation can be achieved in the hadronic decay channels through a complete set of observables including the determination of the initial τ direction. This new information, as compared to standard analyses, is obtained through a kinematic reconstruction complemented by the precision measurement of the charged particles using the microvertex detector in order to remove part of the intrinsic ambiguity of the method.

5.2 Event selection and decay classification

5.2.1 τ-pair selection

This analysis is based on a global event selection that retains τ pair candidates from Z decays. Each event is divided into two hemispheres along the thrust axis. The τ event selection is described in [17] and references therein. The method is based on the removal of non-τ background identified as Bhabha, mu-pair, hadronic, photon-photon induced, and cosmic ray events. A well-tested procedure of reconstructing the spatial energy flow [10] is used in order to include all the energy measurements and their topology in the detector.

However, to enhance the selection efficiency and to reduce the biases in the polarisation measurement, some minor modifications of the usual cuts [17] are introduced:

- cuts against $\gamma\gamma$ events and the cut on the energy of the leading tracks in both hemispheres against Bhabha and di-muon events are not applied when both hemispheres are identified to be hadronic.
- in order to reduce the contamination from $\gamma\gamma \to \tau\tau$ and $\gamma\gamma \to q\bar{q}$ background, events with one hemisphere with a single charged hadron and no π^0 are removed if $|\cos\theta| > 0.792$ and $x < 0.088$.
- hadronic cuts are loosened taking advantage of the more precise hadronic mass determination after π^0 reconstruction, rather than relying on the energy-flow variables used in the selection.

5.2.2 Particle identification

A likelihood method for charged particle identification incorporates the relevant information from the detector. In this way, each charged particle is assigned a set of probabilities from which a particle type is chosen. A detailed description of the method can be found in [19] and [22].

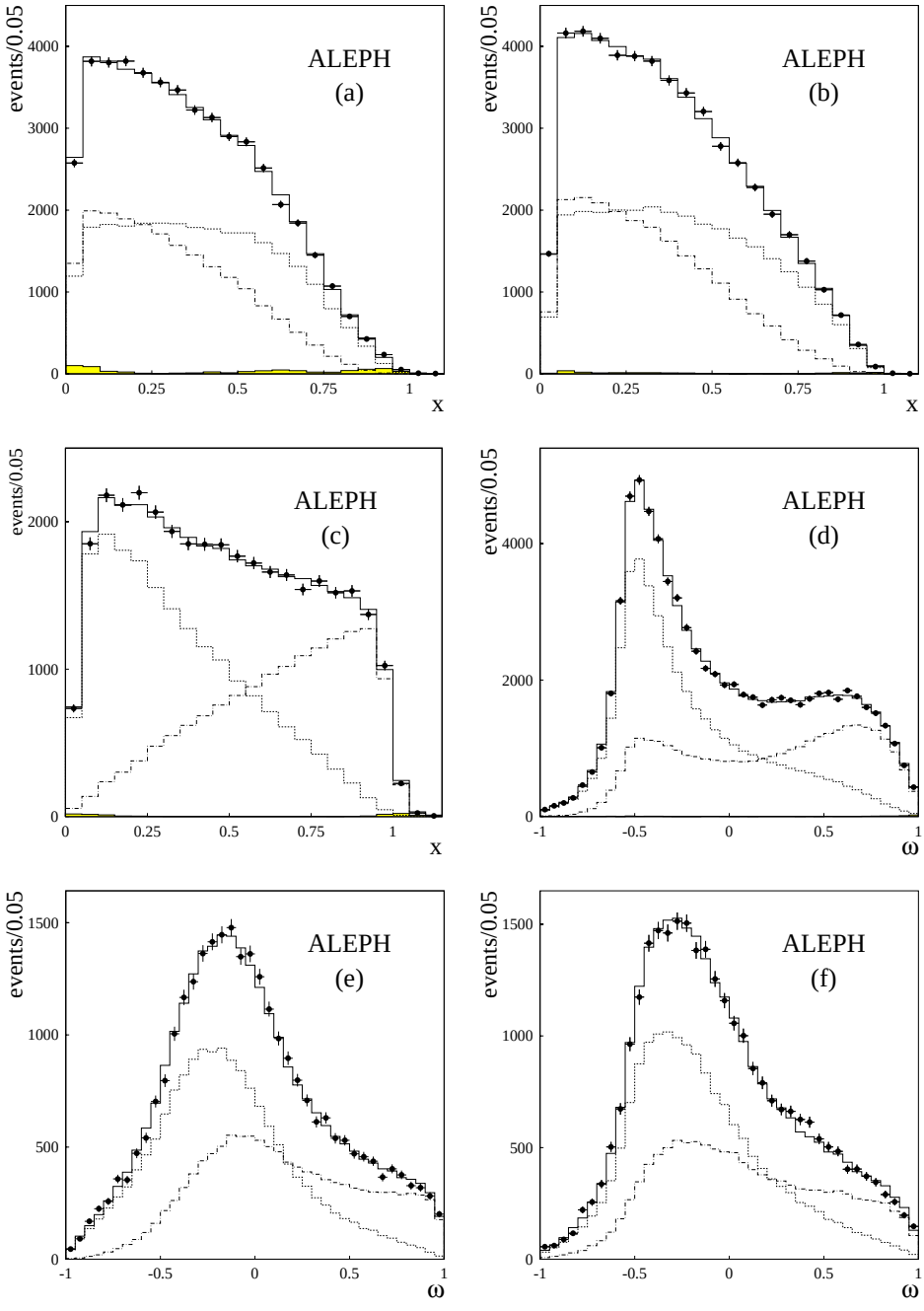

Fig. 13a–f. Distributions of the x variable for $\tau \to e\nu\bar{\nu}$ **a**, $\tau \to \mu\nu\bar{\nu}$ **b**, and $\tau \to h\nu$ **c**. Distributions of the ω variable for $\tau \to \rho\nu$**d** and $\tau \to a_1\nu$: $a_1 \to 3h$**e** and $a_1 \to h2\pi^0$**f**. The dotted and dash-dotted lines correspond to the contributions of left- and right-handed τ's respectively. The shaded area is the non-τ background contribution

Briefly, the particle identification is based on the following information: *(i)* the dE/dx in the TPC, *(ii)* the longitudinal and transverse shower profile in the ECAL near the extrapolated track, and *(iii)* the energy and the average shower width in the HCAL, together with the number of planes, out of the last ten of the HCAL, which had fired, and the number of hits in the muon chambers. Because of the calorimetric requirements, the complete identification method is only applied to particles with momenta larger than 2 GeV/c.

The performance of the identification method has been studied in detail using samples of leptons from Bhabha, μ-pair, and two-photon events, and hadrons from π^0-tagged hadronic τ decays. All data sets cover the full angular and momentum range [17,19]. Ratios of particle identification efficiencies in the data and the corresponding Monte Carlo samples are obtained as a function of momentum. They are then used to correct the Monte Carlo efficiencies in the $\tau^+\tau^-$ sample, thus taking into account the different momentum distributions and particle environment. Misidentification probabilities are obtained in the same way. The results of these analyses were already given for the 1990-1993 data [19]. Figures 15 and 16 show the corresponding efficiencies and misidentification probabilities measured in the 1994-1995 data.

Table 6 gives the efficiency matrix for one-prong τ decays used for this analysis, i.e., for particles with a momentum larger than 2 GeV/c and not in a crack region

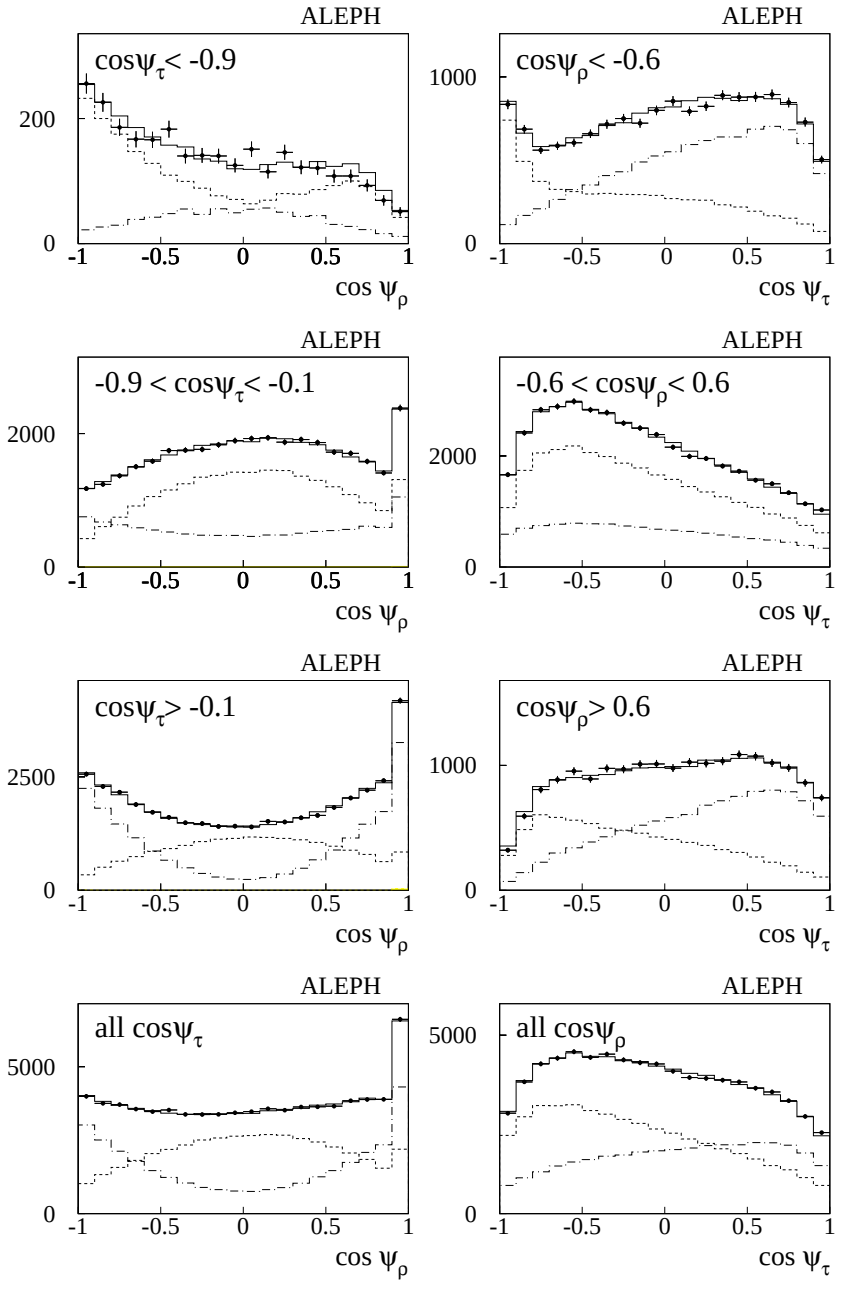

Fig. 14. Distributions of the two decay angles in the $\tau \to \rho\nu$ channel. The vertical axes are in unit of events/0.1. The dotted and dash-dotted lines correspond to contributions of left- and right-handed τ's respectively. The non-τ background contribution is negligible

between ECAL modules. The 2 GeV/c cut is not applied to electron candidates because of the good dE/dx separation at low momentum, while the crack veto is not required for muons which are essentially identified in the HCAL. The numbers refer to the 1991-1995 data sample.

5.2.3 Non-τ background

A new method is developed to directly measure in the final data samples the contributions of the major non-τ backgrounds: Bhabhas, $\mu^+\mu^-$ pairs, and $\gamma\gamma \to e^+e^-, \mu^+\mu^-$ events. The procedure does not rely on an absolute normalization for the simulated channels, which is difficult to obtain reliably after the large necessary rejection is ap-

Table 6. Particle identification efficiencies and misidentification probabilities (in percent) in one-prong τ decays as corrected from control data samples. The values are integrated on the corresponding momentum spectra (h refers to the single hadron channel) above 2 GeV/c, excluding the cracks between ECAL modules

Id.↓ True →	e	μ	h
e	99.57 ± 0.07	≤0.01	0.71 ± 0.04
μ	≤0.01	99.11 ± 0.08	0.72 ± 0.04
h	0.32 ± 0.06	0.88 ± 0.08	98.45 ± 0.06
no id.	0.09 ± 0.04	0.01 ± 0.01	0.12 ± 0.03

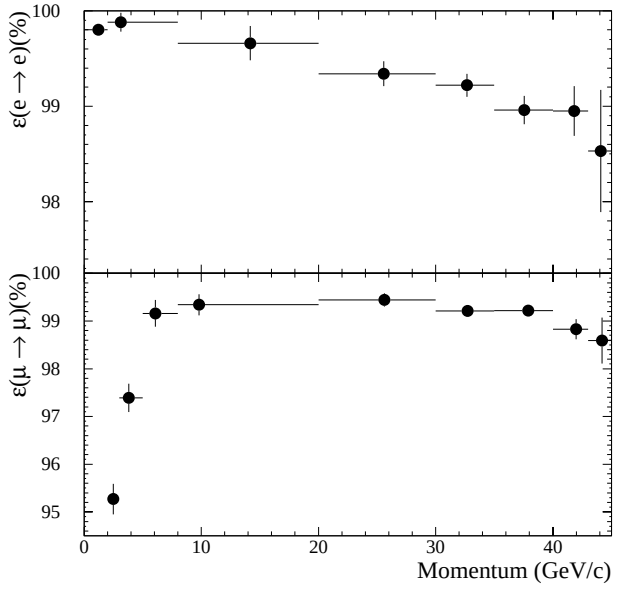

Fig. 15. The identification efficiencies for electrons and muons as a function of momentum for 1994-1995 data (in percent). The efficiencies simulated by the Monte Carlo for the τ sample are corrected by measurements performed on control samples as discussed in the text

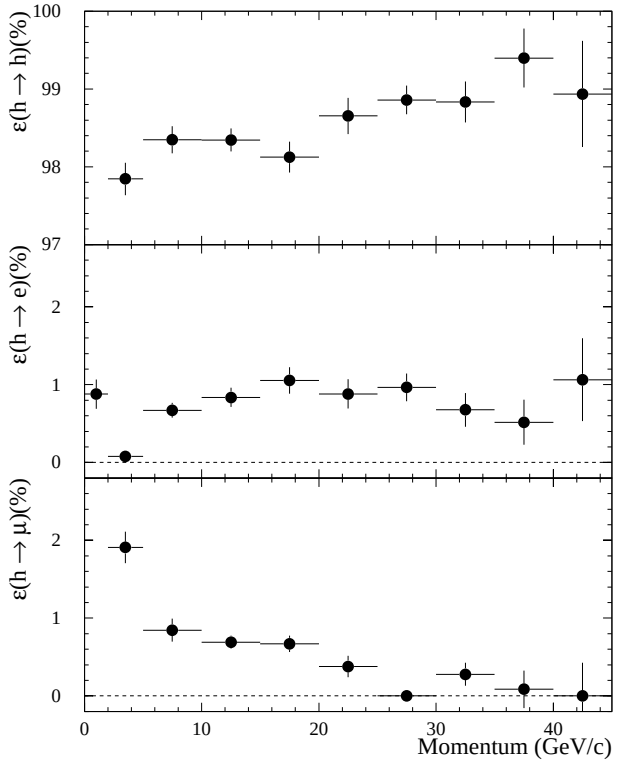

Fig. 16. The identification efficiency and misidentification probabilities for hadrons as a function of momentum for 1994-1995 data (in percent). The values are obtained directly from data using a π^0-tagged hadron sample

plied. It only makes use of a qualitative description of the distribution of the discriminating variables. The basic idea is to apply cuts on the data in order to reduce as much as possible the $\tau\tau$ population while keeping a high efficiency for the background source under study. The background fraction is directly fitted in the cut data sample and then extrapolated to the standard sample.

For Bhabha background, different event topologies are considered in turn. For *e-e* and *e-crack* topologies, the acoplanarity angle (defined by the two tracks azimuthal difference) is required to be larger than 179° or the acollinearity angle (i.e. 180° minus the angle between the directions of the two tracks) should be less than 175° with the difference of transverse energies being less than 3 GeV. The corresponding Bhabha efficiency (compared to the normal sample) is 88% as determined from the simulation. The angular distribution of the restricted sample is then fitted to $\tau\tau$ and Bhabha components (also including a small contribution from the other non-τ backgrounds) from the simulation. Therefore, the Bhabha Monte Carlo input is only used to determine the (large) selection efficiency and the $\cos\theta$ shape inside the final sample, not relying on any determination of the absolute Monte Carlo normalization. The derived Bhabha contribution has a statistical uncertainty which is assigned as a systematic error. Several combinations of variables have been tried, showing a good stability of the result within its error. For the more numerous *e-h* and *h-h* samples, a total energy cut of 55 GeV is applied and the main reduction of τ events is achieved by suppressing true hadrons as compared to electrons misidentified as hadrons: this is done by restricting the opposite hadron in an *e-h* event to have an electron identification probability larger than 0.01 (most of the true hadrons are below this value). A similar approach is used for the *h-h* samples with even tighter identification probability cuts for hemispheres with only one charged hadron (in this case 86% of the hadrons have an electron probability smaller than 0.0002). The Bhabha signal then appears on a distribution of the acollinearity angle between the two hemispheres ($\delta\theta$) at values close to 180°.

A similar technique is used to estimate the μ-pair background. An efficiency of 90% is obtained by requiring an acoplanarity angle larger than 178° for $\mu\mu$ events in the final sample. Here, the fitted distribution is that of the calculated photon energy along the beam for a postulated $\mu\mu\gamma\gamma_{\rm beam}$ kinematics to take the most general case compatible with only the information on the two muons. For μ-*h* and *h-h* final states, the procedure follows the one used for Bhabha background.

The measurement of the $\gamma\gamma$-induced remaining background is based on cuts on the total event energy (typically $E < 35$ GeV, depending on the channels) and the acollinearity angle between the two hemispheres ($\delta\theta < 175°$). The $\gamma\gamma$ background shows up clearly at small overall transverse momentum well above the small τ surviving contribution.

All the above non-τ background contributions are determined on the polarisation data sample with the help of special cuts. The corresponding Monte Carlo generators are only used to compute the efficiency of the cuts. This method is illustrated in Fig. 17 showing the evidence

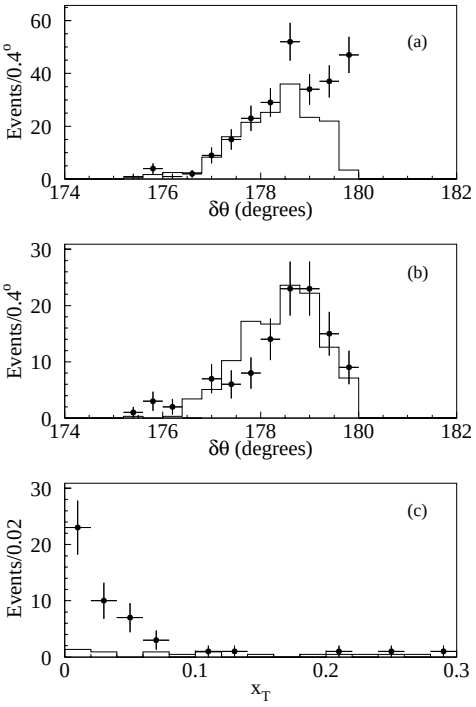

Fig. 17a–c. Distributions in the final ρ sample after applying cuts to reduce the τ contribution and enhance non-τ background (see text for details): **a** acollinearity distribution to enhance Bhabha background; **b** acollinearity distribution to enhance $\mu\mu$ background; **c** total transverse momentum normalized to the centre-of-mass energy to enhance $\gamma\gamma \to$ *hadrons* background. The histograms give the respective τ contributions as expected from the simulation

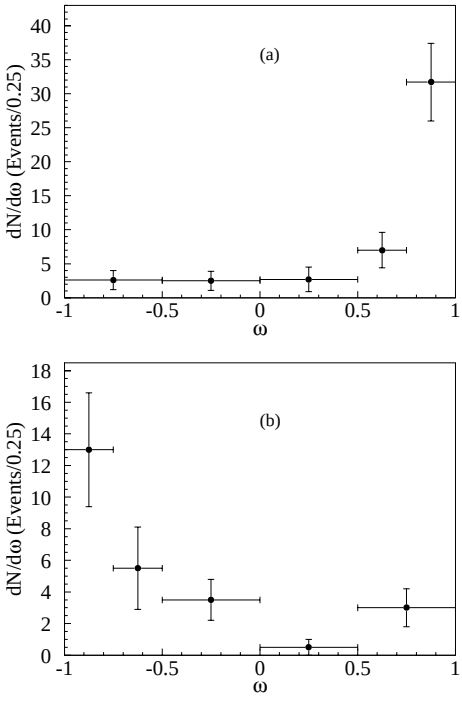

Fig. 18a,b. Distributions of the ω variable in the final ρ sample after applying cuts to reduce the τ contribution and enhance non-τ background (see text for details): **a** Bhabha background; **b** background from $\gamma\gamma \to$ *hadrons*. In both cases the small remaining τ contribution estimated from the simulation has been subtracted out

for Bhabha and $\gamma\gamma \to \tau\tau$ or $q\bar{q}$ backgrounds in the $\rho\nu$ channel, the contribution from $\mu\mu$ being negligible in this case.

As an important bonus, this procedure leads to a determination from data alone of the background distributions which are relevant for the polarisation measurement. This method is preferable to using the Monte Carlo predictions which are questionable in view of the large rejection factors achieved. Distributions of the ω variable obtained in the $\rho\nu$ channel are given in Fig. 18.

As in the analysis of Sect. 4, cosmic ray background is determined to be very small after the additional cuts [19]. The contamination from hadronic Z decays affects only the hadronic channels. Its small contribution is estimated with the JETSET 7.4 generator [24]. Tests were previously made to ascertain the reliability of the prediction for the rate of surviving low multiplicity events by comparing to data [17]. A 30% uncertainty was derived from these tests.

The non-τ background contributions are given in Table 7, separately for the considered channels.

5.2.4 Photon and π^0 reconstruction

As in the previous analysis, the photon and π^0 reconstruction is performed according to a likelihood method in which several estimators and probabilities are computed in order to distinguish between genuine and fake photons produced by hadronic interactions in ECAL or by electromagnetic shower fluctuations [17].

An algorithm is used to form photon pairs in each hemisphere [17] using a π^0 estimator $D^{\pi^0}_{i,j} = P_{\gamma_i} P_{\gamma_j} P_{\pi^0_{i,j}}$ for two photons i and j, where $P_{\pi^0_{i,j}}$ is the probability from a kinematic π^0-mass constrained fit. A good agreement between data and Monte Carlo is observed for the distributions of $P_{\pi^0_{i,j}}$ and $D^{\pi^0}_{i,j}$. Figure 19 shows the corresponding π^0 mass distributions with the expected contribution from photon pairs including at least one fake photon.

High-energy π^0's with overlapping photon showers are reconstructed through an analysis of the spatial energy deposition in the ECAL towers ("unresolved π^0's"). All the remaining single ("residual") photons are then considered and those with $P_\gamma > 0.5$ are selected as π^0 candidates. The P_γ distributions are given in Fig. 20 for all photons and for the residual ones after renormalizing the amount of fake photons in the simulation by a factor depending on the τ decay hadronic final state and ranging from 1.17 to 1.28. The shapes in data and Monte Carlo are in good agreement. The energy dependence of the data distributions is also well reproduced by the simulation: hence the photon efficiencies resulting from the $D^{\pi^0}_{ij}$ and P_γ cuts are adequately described by the Monte Carlo, as already observed in Sect. 4.4.2 and Fig. 7.

Table 7. Channel identification efficiencies and contaminations as measured on the data for the τ direction method. The efficiency includes a geometrical acceptance factor of 0.86. "acol" refers to the sample of events with a leptonic τ decay, where information from the acollinearity angle [2,23] is used

Channel	h	ρ	$3h$	$h2\pi^0$	e	μ	$acol$
candidates	33350	78553	25287	28757	52952	50249	85035
efficiency (%)	63.1	69.1	62.9	57.5	68.7	74.8	74.4
τ back. (%)	7.3	9.1	3.9	20.7	0.7	1.0	0.7
Bhabha	57 ± 10	118 ± 40	-	9 ± 5	383 ± 66	-	187 ± 37
$\mu\mu$	20 ± 5	16 ± 14	-	2 ± 2	10 ± 3	212 ± 55	94 ± 24
$q\overline{q}$	61 ± 30	205 ± 69	72 ± 35	37 ± 15	8 ± 4	-	8 ± 4
$\gamma\gamma ee$	-	-	-	2 ± 3	187 ± 45	-	91 ± 20
$\gamma\gamma\mu\mu$	7 ± 7	-	-	-	7 ± 5	241 ± 57	106 ± 24
$\gamma\gamma\tau\tau + \gamma\gamma q\overline{q}$	15 ± 10	31 ± 11	0 ± 4	3 ± 5	22 ± 6	22 ± 6	28 ± 7

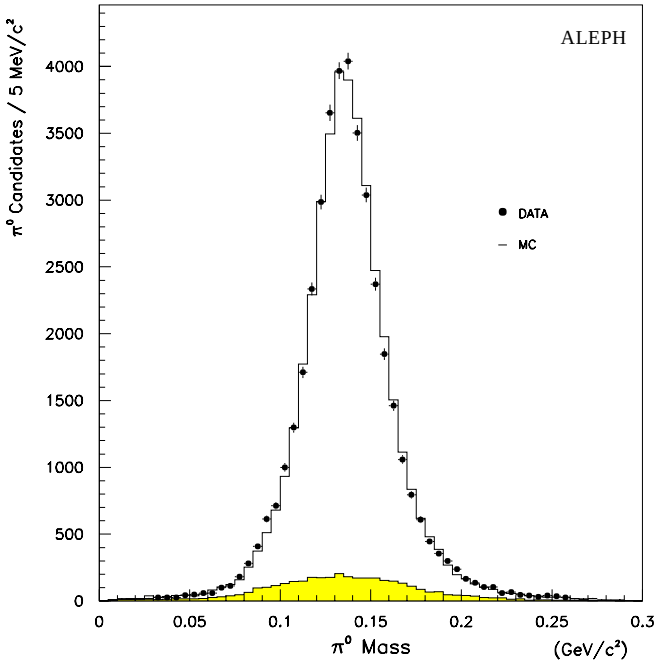

Fig. 19. Photon-pair mass distribution for reconstructed π^0 candidates. Data (points) are compared to the simulation (histogram). The shaded histogram gives the simulated contribution where at least one of the photons is fake

Finally, photon conversions are identified following the procedure described in [17]. They are added to the list of good photons and included in the π^0 reconstruction. The fractions of resolved, unresolved and residual π^0's are presented in Fig. 21 as a function of the π^0 energy. It is seen that the data distributions are well reproduced by the simulation. The fraction of resolved "calorimetric" π^0's remains significant out to large energies in this analysis as compared to the previous one (see Sect. 4.3.3 and Fig. 4); this effect is the result of a looser π^0 definition here, where highly asymmetric $\gamma\gamma$ pairs are more likely to be counted as resolved π^0's, whereas they would be identified as unresolved in the other method because of the tight invariant mass cut.

5.2.5 Decay classification

τ decays are classified according to the number of charged tracks and their identification, and the number of reconstructed π^0's. Beyond the classification achieved in the previous analyses [17,19–21] some additional cuts have been developed in order to reduce the ρ and K^* background level in the h channel, as explained below.

In order to reject ρ decays where the π^0 is close to the charged pion and undetected as such, the sum of the energies in the first two stacks of ECAL is required to be less than 75% of the charged pion momentum. The energy is measured including all the pads in a cone of 30° around the track. To further reduce the ρ contamination, the hemispheres with one charged hadron and a single residual photon with a probability P_γ greater than 0.2 are rejected.

The K^* (decaying into $K^0_L\,\pi$) component is reduced by a cut on the HCAL energy deposit ($E_{\rm hcal}$) and the azimuthal offset ($\delta\phi$) between the track impact and the energy weighted barycentre of the energy deposit in HCAL [25]. The cut is applied on the following variables:

$$\delta_E = \frac{E_{\rm hcal} - P_h}{\sigma_h} \tag{7}$$

$$\delta\phi = \xi\ |\phi_{\rm barycentre} - \phi_{\rm track\ impact}| \tag{8}$$

where P_h is the hadron momentum and σ_h the corresponding HCAL energy resolution. The value of the parameter ξ is $+1$ if $\phi_{\rm barycentre}$ is in the direction of the charged hadron bending, and -1 otherwise. The following region in the $(\delta_E\ , \delta\phi)$ plane is cut:

$$\begin{cases} \delta_E > 0 \\ \delta\phi < -1^\circ \\ \delta\phi < (\frac{2}{3}\delta_E - 3)^\circ\ . \end{cases}$$

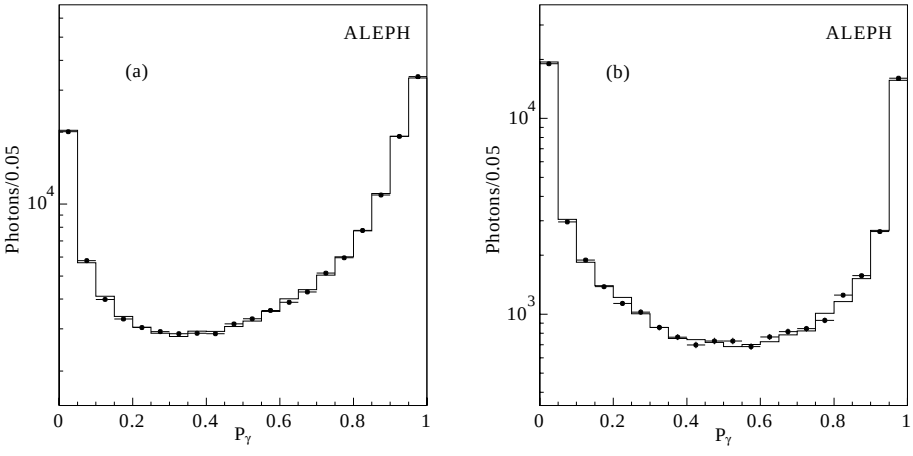

Fig. 20a,b. Photon estimators used to distinguish between genuine and fake photons ($P_\gamma = 1$ corresponds to the case of genuine photons): **a** estimators for photons used in resolved π^0 reconstruction (the photon energy is not used), **b** estimators for residual photons (using the photon energy). Data (points) are compared to the simulation (histogram)

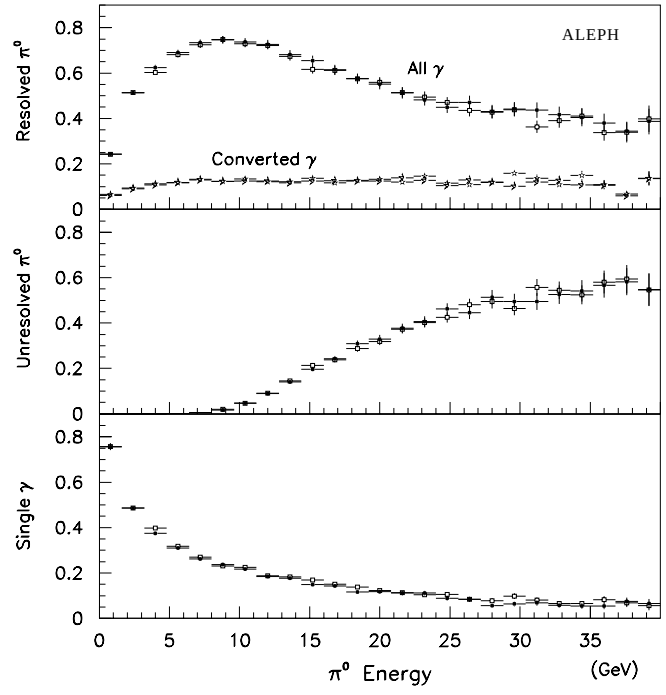

Fig. 21. Fractions of different π^0 types as a function of the π^0 energy. The points represent the data and the open squares the simulation. Also indicated with stars are the fractions for resolved π^0 containing at least one converted photon

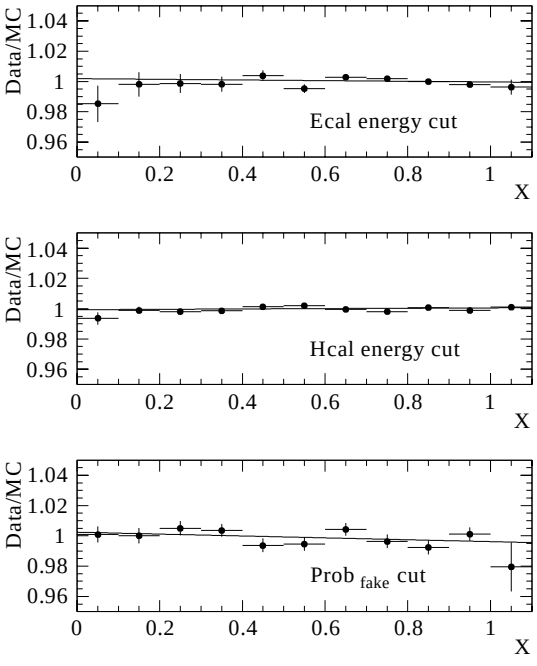

Fig. 22. The energy dependence of the ratio of data to Monte Carlo efficiencies for the additional cuts in the pion channel in the 1991-1995 data

In order to verify that those supplementary cuts do not introduce biases into the measurement of the τ polarisation, the ratio of the efficiencies for each of the three cuts on data and on Monte Carlo, $\epsilon_{\text{data}}/\epsilon_{\text{MC}}$, is studied as a function of the pion momentum (Fig. 22). The computation of these efficiencies and of their statistical errors takes into account the non-pion background estimated by Monte Carlo. The small bias introduced by these cuts is evaluated by a linear fit and corrected in the final polarisation measurement. The corresponding statistical error is taken as a systematic uncertainty.

For the ρ channel, a cut on the invariant mass is required, $m_\rho > 0.4$ GeV/c^2, to reduce the feedthrough from the h mode. For the a_1 channel, the invariant mass is required to be less than the τ mass. In the case of a decay into three charged hadrons ($3h$), three good tracks are required in the hemisphere.

The channel identification efficiencies, the τ background, and the non-τ background contributions as measured in the data (except for $q\bar{q}$) are shown in Table 7.

5.3 The τ direction

5.3.1 Kinematic reconstruction of the τ direction

For events where both τ's decay into hadrons (called hadronic events), it is possible to reconstruct the $\tau^+\tau^-$ direction, thereby enhancing the sensitivity of the polarisation measurement in the ρ and a_1 channels as seen in Sect. 2. This method is used here for the first time.

Table 8. Sensitivities obtained in the ρ and the a_1 channels, for various methods using the true or the reconstructed direction. Only events with two reconstructed directions are considered here

method	ρ-*had*	$a_1(3\pi)$-*had*	$a_1(\pi 2\pi^0)$-*had*
$\omega_{\rm true}$, without $\vec{\tau}$	0.48 ±0.01	0.41 ±0.01	0.41 ±0.01
$\omega_{\rm true}$, with $\vec{\tau}$	0.57 ±0.01	0.57 ±0.01	0.56 ±0.01
$\omega_{\rm rec}$, without $\vec{\tau}$	0.46 ±0.01	0.40 ±0.01	0.37 ±0.01
$\omega_{\rm rec}$, with $P_1 = P_2 = 0.5$	0.51 ±0.01	0.47 ±0.01	0.42 ±0.01
$\omega_{\rm rec}$, with $P_{1,2}$	0.51 ±0.01	0.48 ±0.01	0.43 ±0.01

In hadronic events, although the momentum of each neutrino is unknown, the τ direction can be determined up to a twofold ambiguity. The two solutions lie at the intersection of the cones having for axis the hadronic direction in each hemisphere and an opening angle ϕ_0 computed from the measured hadron momentum P_h and energy E_h, assuming the pion mass for each individual hadron,

$$\cos\phi_0 = \frac{2E_\tau E_h - {m_\tau}^2 - {m_h}^2}{2P_\tau P_h} \ , \qquad (9)$$

where P_τ and E_τ are the energy and the momentum of the parent τ assumed to be produced at the beam energy, and m_h the hadronic mass.

A procedure is used for events where the cones do not intersect, mainly because of detector resolution effects. The hadron momenta are allowed to fluctuate within the expected resolutions of charged and neutral pions. The τ direction is taken as the average of the found solutions among the random trials, provided at least 10 solutions are found for 500 trials. This procedure attributes a τ direction to half of the events where the two cones are not initially intersecting.

As a result, 80% of the hadronic events are available for the polarisation analysis using the τ direction. The remaining 20% without a reconstructed direction are analysed in the standard way. On the whole 52% of the $\tau \to \rho\nu$ decays benefit from this improvement.

5.3.2 Handling the two τ directions

Since the typical τ decay length is 2 mm at LEP I, the precise determination of the secondary charged tracks brings some information allowing in principle to lift the twofold ambiguity and to choose the actual τ direction. This procedure stems from the 3-dimensional method developed for the measurement of the τ lifetime [6]. In practice one can only separate the two solutions on a statistical basis with the help of an estimator, D_h, and assign to each of the two directions a probability $P_{1,2}$ to be the true one. This procedure is explained in Appendix A, while more details can be found in [26].

Reference distributions for the estimator are set up with Monte Carlo for various event configurations (π-π, ρ-ρ, ρ-π, etc.) and probabilities $P_{1,2}$ for each of the two found τ directions to be the true one are obtained.

If the highest probability is retained, it is found by simulation that the closest of the two directions to the true one is chosen in 65% of the cases for all channels combined. A more relevant way to characterize the procedure is to consider the precision achieved on the τ direction. While the mean value of the angle between the two directions is 24 mrad, the angle between the direction with the higher probability and the true one is 12 mrad on average. The corresponding value for the direction closest to the true one is 7 mrad (dominated by resolution effects) and a value of 15 mrad is obtained if a random choice between the two solutions is made. In practice, the two solutions are retained, with their respective probabilities.

5.3.3 Analysing the polarisation with the τ direction

The polarisation is analysed in each hemisphere using the proper optimal variables, $\omega_{1,2}$, calculated for the observed decay for each choice of direction using the description of the hadronic system given in [8]. Both directions are entered into the expected decay distribution depending on P_τ:

$$\begin{aligned} W &= P_1 F(\omega_1)(1 + P_\tau\omega_1) + P_2 F(\omega_2)(1 + P_\tau\omega_2) \\ &= \tilde{F}(1 + P_\tau\omega) \end{aligned} \qquad (10)$$

with the new optimal observable

$$\omega = \frac{P_1 F(\omega_1)\omega_1 + P_2 F(\omega_2)\omega_2}{P_1 F(\omega_1) + P_2 F(\omega_2)} \ . \qquad (11)$$

The ideal sensitivity given in Table 1 is naturally degraded by detector resolution effects and mostly by the imperfect determination of the τ direction. The expected sensitivities are given in Table 8 from a Monte Carlo study. The gain in sensitivity using the calculated probabilities instead of affecting each direction with an *a priori* 50% weight is quite small, but it provides the ultimate gain in precision achievable within the ALEPH detector capabilities.

For events where one of the τ's decays leptonically and for which the information on the τ direction cannot be retrieved, the acollinearity angle between the decay products in the two hemispheres contains additional information as compared to the separate analysis of single decays. This method [2,23] is also used in this analysis.

5.4 Summary of systematic effects

Possible sources of systematic effects come from the τ selection, particle identification, and π^0 reconstruction. The dominant systematic uncertainties are due to photon identification and π^0 reconstruction, the non-τ background, and, in the case of the a_1 modes, the dynamics of the decay. Table 9 shows the summary of the main components of the systematic uncertainties for A_τ and A_e.

The particle identification efficiency matrix is measured as a function of momentum using data samples of

Table 9. Summary of systematic uncertainties (%) for A_τ and A_e with the τ direction method

	A_τ						
Systematic effect	h	ρ	$3h$	$h2\pi^0$	e	μ	*acol*
eff. $h \to h$ id.	0.17	0.06	-	0.06	0.20	0.35	0.01
misid. $(e,\mu) \to h$	0.24	0.05	-	0.09	0.13	0.25	0.57
$\tau\tau$ selection	0.13	0.03	0.01	0.01	0.03	0.04	-
τ BR and back.	0.04	0.05	0.03	0.09	0.01	0.02	0.02
tracking	0.08	0.07	0.22	-	-	0.21	0.30
γ-reconstruction	-	0.22	0.29	0.66	-	-	-
π^0-reconstruction	0.11	0.29	0.68	0.62	-	-	-
fake photons	0.31	0.17	0.28	0.75	-	-	-
ECAL scale	-	0.20	0.33	0.63	0.15	-	-
ECAL + HCAL cut	0.22	-	-	-	-	-	-
modelling	-	-	0.68	0.68	-	-	-
non-τ back.	0.24	0.16	0.07	0.05	0.73	0.50	0.60
τ MC statistics	0.34	0.30	0.61	0.77	0.73	0.80	1.44
TOTAL	0.66	0.57	1.30	1.70	1.07	1.06	1.69

	A_e						
Systematic effect	h	ρ	$3h$	$h2\pi^0$	e	μ	acol
tracking	0.04	-	-	-	-	0.05	-
non-τ back.	0.13	0.08	0.02	0.07	1.23	0.24	0.24
modelling	-	-	0.40	0.40	-	-	-
TOTAL	0.13	0.08	0.40	0.41	1.23	0.24	0.24

kinematically identified particles, as described in Sect. 5.2.2. The procedure yields both the relevant efficiencies and their associated uncertainties which are dominated by the statistics of the control samples. The effect of this systematic uncertainty on the polarisation measurement is significant only for the e or μ channels.

To study the effect of the τ pair event selection, the difference in the selection efficiency between data and the Monte Carlo is analysed for each cut, as discussed in detail in [17,19]. The systematic error on the selection has a significant effect only on the h channel where the nearly flat momentum distribution is distorted at low values by the $\gamma\gamma$ cuts and for large momenta by the Bhabha and μ-pair cuts.

The branching ratios used in the Monte Carlo are corrected using the measured values of ALEPH [17,19] and the uncertainty in the amount of feedthrough in a given τ decay channel from the other modes is obtained by varying the branching ratios within the errors given in [17,19], taking into account the correlations between them. The impact on the τ polarisation measurement is negligible.

The tracking resolution affects only the a_1 decay since three reconstructed charged hadrons are required. In this decay the tracks are generally close to each other and therefore partially overlap. A reconstruction problem could occur if the two same-sign tracks have nearly the same transverse momentum. Data and Monte Carlo distributions of the angle between the two tracks at the vertex are in fact in agreement within statistics and a systematic uncertainty for the polarisation is derived. The systematic error on the momentum calibration is also estimated with the largest effect observed on the μ channel.

A complete investigation of the observables entering photon and π^0 reconstruction is undertaken. For each variable a comparison between data and Monte Carlo is performed in order to search for possible systematic deviations. These differences are then injected in the complete reconstruction procedure, affecting both the number of events in a given channel and the corresponding ω distributions. Each data-Monte Carlo comparison yields a systematic uncertainty limited by the statistics of the data. As discussed in full detail in [17], these studies include the effect of the clusterization algorithm, the photon probabilities, the threshold energy cut for low energy photons or the minimal distance between a charged track and a photon in the electromagnetic calorimeter. Similarly, the effect of the cuts on the π^0 estimators is also determined. All the contributions to the total systematic uncertainties for this source are added in quadrature.

Another source of uncertainty in the photon and π^0 treatment is due to the problem of fake photons generated by hadron interactions in ECAL or electromagnetic shower fluctuations. This source of photon candidates is underestimated in the Monte Carlo simulation with respect to the data. This deficit produces a bias on the polarisation measurement and needs to be corrected for with the systematic uncertainty carefully estimated. In general, the effect has been studied by removing fake photons in the simulation and repeating the analysis: decay classification and polarisation determination in all channels. This method establishes the sensitivity of the measurement to the problem. Then the fake photon deficit in the simulation is measured in all the needed hadronic channels by fitting probability distributions in data and Monte Carlo as discussed in Sect. 5.2.4 and the corresponding systematic uncertainties are deduced.

A more direct method is used in the h channel for the events with a residual photon where a tighter probability cut was applied to reject more ρ background (see Sect. 5.2.5). Since the ρ contribution can be well estimated by Monte Carlo, it is possible to use the results of this cut both on data and Monte Carlo to estimate the relative effect of fake photons as a function of momentum. Any momentum dependence of the Monte Carlo deficit would produce a bias for the polarisation. Such a bias is measured (Fig. 22) and the statistical uncertainty in the linear momentum fit is taken as systematic error. This procedure in the h channel does not take into account the loss of events with multiple fake photons entering the definition of π^0 candidates. A special study was made to estimate this effect as the simulation tends to underestimate the fake photon multiplicity, with the result that the effect on the polarisation is small compared to that of residual photons.

Since some additional calorimetric cuts are introduced in order to further reduce the level of the ρ and K^* background in the hadron channel, it is important to study

Table 10. $\mathcal{A}_e$ and $\mathcal{A}_\tau$ results with statistical and systematic uncertainties for the 1990-1995 data with the τ direction method

Channel	$\mathcal{A}_\tau$ (%)	$\mathcal{A}_e$ (%)
hadron	$15.49 \pm 1.01 \pm 0.66$	$17.36 \pm 1.35 \pm 0.13$
rho	$13.71 \pm 0.79 \pm 0.57$	$15.04 \pm 1.06 \pm 0.08$
a1(3h)	$15.01 \pm 1.55 \pm 1.30$	$15.78 \pm 2.07 \pm 0.40$
a1(h2π^0)	$15.94 \pm 1.73 \pm 1.70$	$12.65 \pm 2.31 \pm 0.41$
electron	$14.58 \pm 2.18 \pm 1.07$	$16.67 \pm 2.92 \pm 1.23$
muon	$14.45 \pm 2.13 \pm 1.06$	$12.05 \pm 2.78 \pm 0.24$
acollinearity	$13.34 \pm 3.83 \pm 1.80$	$19.41 \pm 5.02 \pm 0.24$
Combined	$14.58 \pm 0.53 \pm 0.39$	$15.50 \pm 0.71 \pm 0.11$

their effect on the hadron momentum distribution. The results have been presented in Sect. 5.2.5 and the corresponding systematic uncertainties derived.

Finally, the effect on the A_τ and A_e measurements from the different sources of non-τ background has been studied in detail directly on the data with the method presented in Sect. 5.2.3. This procedure allows the energy distribution of the remaining Bhabha events in the selected sample to be investigated and a direct measurement of their $\cos\theta$ distribution to be made. The latter information is particularly relevant for the A_e determination because of the asymmetric Bhabha contamination. Using as input the distributions derived from data with their statistical and systematic uncertainties, their impact on A_e and A_τ is assessed. It is important to note that the dominant statistical uncertainty affects both the normalization of the background and the shape of the ω and $\cos\theta$ distributions. The most seriously affected channel is clearly that of the electron, both for A_τ and A_e.

5.5 Results

Table 10 gives the results for $\mathcal{A}_e$ and $\mathcal{A}_\tau$ in the seven channels considered in this analysis. The statistical and systematic uncertainties are given separately. The last line presents the combination of these results taking into account their correlations, including the polarisation correlation between the two hemispheres in an event.

Figures 23, 24, and 25 show the ω distribution for the ρ and a_1 decay modes. The ω distributions for the decays where it was possible to reconstruct the τ direction are also shown separately.

6 Combined results

6.1 Standard model corrections

The A_τ and A_e parameters are obtained by fitting the integral, in each $\cos\theta$ bin, of the function (1) to the measured polarisation. To obtain the combinations of effective couplings ($\mathcal{A}_l$) related to $\sin^2\theta^{\rm eff}_{\rm W}$, corrections have to be applied which take care of the fact that the polarisation was not measured at the Z pole and that there are radiative corrections and Z-γ interference effects. These corrections are computed by the ZFITTER program [4] in the following way.

For a set of the standard model parameters (Z mass, top mass, Higgs mass, α_s), ZFITTER provides the value of the effective couplings in the framework of the standard model. Cuts are defined on acollinearity and momentum which reproduce the ones used in the analysis. Then the $\mathcal{A}_{fb}$ asymmetry, and the polarisation in each $\cos\theta$ bin are calculated at the given energy. The same fitting procedure as for the data is applied and the difference between the effective couplings and the fitted parameters is taken as the correction.

The study of the stability of the corrections against the variation of the input parameters within their errors shows that the related error is negligible compared to the systematic errors involved in the analyses. The same is true for the values chosen for the cuts. With this procedure, the inaccuracy of (1) in describing the polarisation does not introduce any bias but may simply reduce very slightly the sensitivity. The level of these corrections is 0.04% with an uncertainty of 0.01%. It has been checked that using as input the measured values of $\mathcal{A}_{fb}$ gives the same results.

6.2 Consistency and combination of the results

To investigate the consistency of the two analyses, both statistical and systematic effects have to be taken into account.

As a result of the different selection procedures, there is a significant number of events which belong to only one of the two samples. The fractions of unshared events in the different channels, averaged over the full angular distribution, are 24% (π), 27% (ρ), 24% ($a_1 \to 3\pi$), 47% ($a_1 \to \pi 2\pi^0$), 24% (e), and 13% (μ). Typically, these fractions are by a factor 1.6 larger in the small-angle region ($|\cos\theta| > 0.7$) than in the central part. The distribution of the events has to be taken into account in the evaluation of the consistency and in the combination of the measurements since this small-angle region has a significant contribution to the $\mathcal{A}_e$ determination. Another statistical effect comes from the channels where the τ direction is taken into account since different information is used in the two analyses. Finally, the Monte Carlo samples do not completely overlap.

The systematic effects of the two methods have in common the detector behaviour and the basic event reconstruction; however the analysis tools used are largely independent. Furthermore, the procedures developed to measure efficiencies, and various corrections are different in the two analyses and thus a part of the estimated systematic uncertainties is uncorrelated.

The $\mathcal{A}_\tau$ values given by the two analyses - for each channel and globally - are in agreement within the estimated uncertainties. The combination of all channels, gives $\Delta\mathcal{A}_\tau = (0.14 \pm 0.52)\%$, where the statistical and systematic part of the error are comparable. The agreement

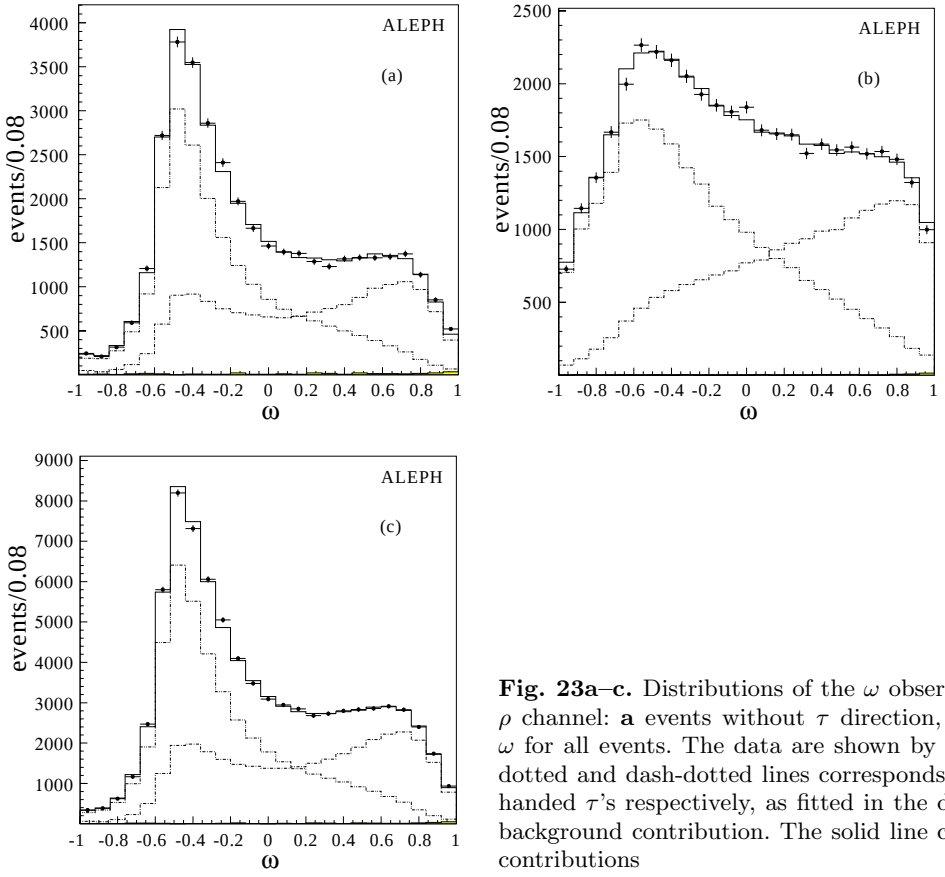

Fig. 23a–c. Distributions of the ω observable used in the polarisation fit of the ρ channel: **a** events without τ direction, **b** events with τ direction, **c** standard ω for all events. The data are shown by points with statistical errors bars. The dotted and dash-dotted lines corresponds to the contributions of left- and right-handed τ's respectively, as fitted in the data. The shaded area shows the non-τ background contribution. The solid line corresponds to the sum of all simulated contributions

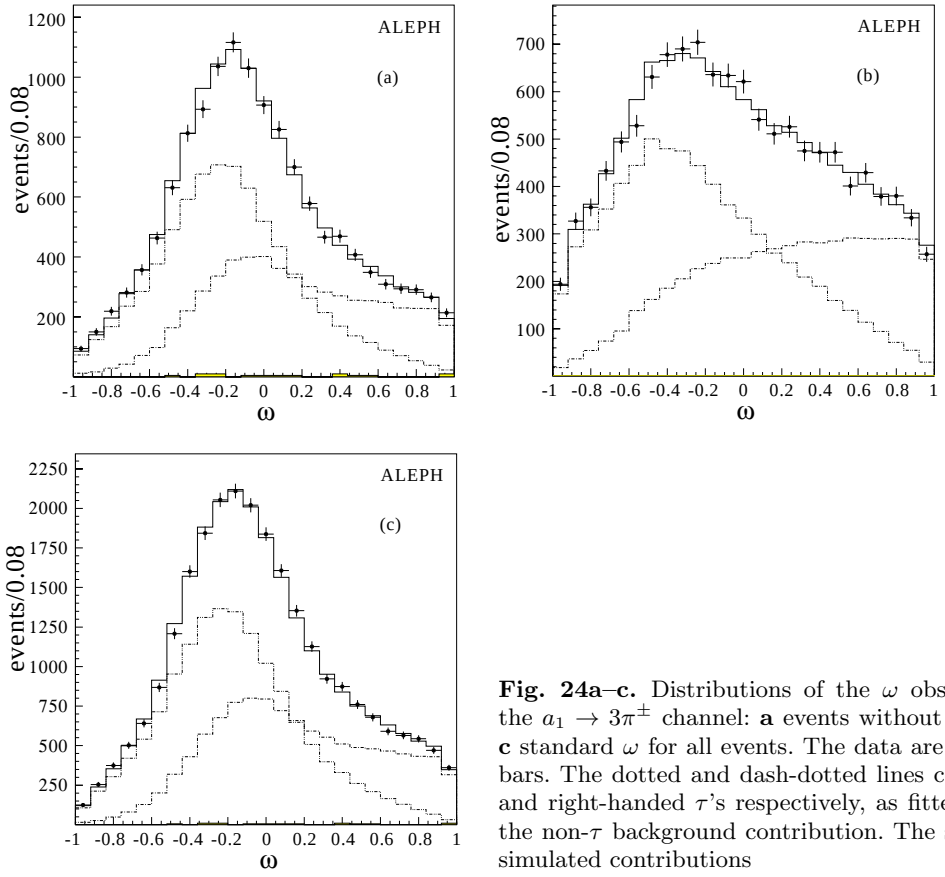

Fig. 24a–c. Distributions of the ω observable used in the polarisation fit of the $a_1 \to 3\pi^{\pm}$ channel: **a** events without τ direction, **b** events with τ direction, **c** standard ω for all events. The data are shown by points with statistical errors bars. The dotted and dash-dotted lines corresponds to the contributions of left- and right-handed τ's respectively, as fitted in the data. The shaded area shows the non-τ background contribution. The solid line corresponds to the sum of all simulated contributions

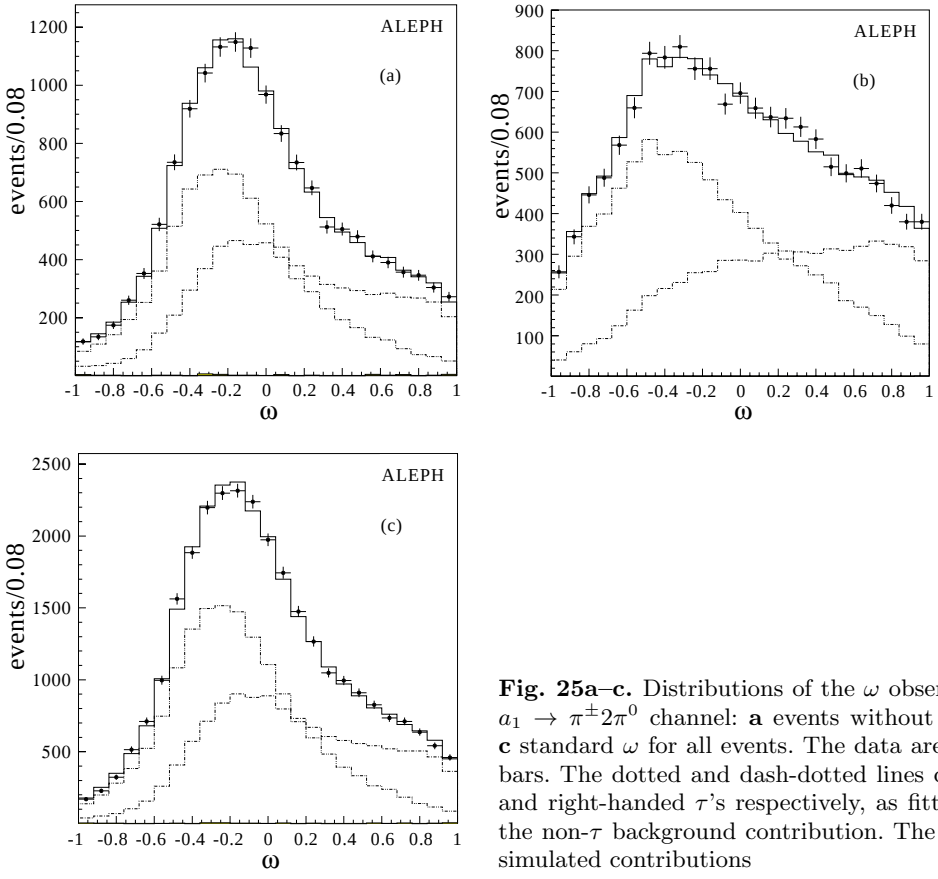

Fig. 25a–c. Distributions of the ω observable used in the polarisation fit of the $a_1 \to \pi^{\pm}2\pi^0$ channel: **a** events without τ direction, **b** events with τ direction, **c** standard ω for all events. The data are shown by points with statistical errors bars. The dotted and dash-dotted lines corresponds to the contributions of left- and right-handed τ's respectively, as fitted in the data. The shaded area shows the non-τ background contribution. The solid line corresponds to the sum of all simulated contributions

is not as good in the case of the $\mathcal{A}_e$ measurement where the deviation between the two analyses, mainly due to the hadron channel, is $\Delta\mathcal{A}_e = (0.92 \pm 0.48)\%$. However, the systematic uncertainties on $\mathcal{A}_e$, dominated by the effect of the non-τ background (chiefly Bhabha events), are smaller by a factor of 5-10 than the statistical errors, and the many cross-checks performed show that the background levels and distributions are known within the quoted uncertainties. This lead to the conclusion that the observed difference is the result of a statistical fluctuation.

6.3 Final results

The consistency of the two sets of results having been checked, they are combined to obtain the final results. Since the two analyses have comparable statistical and systematic uncertainties, the combination procedure is not a critical one. It was chosen to average the results using equal weights. For the computation of the final errors the statistical correlation between the two samples is taken into account together with the systematic uncertainty correlations.

The results are given in Table 11 for all the analysed modes and in Table 12 for the global values. Figure 26 shows the average tau polarisation as a function of $\cos\theta$.

Table 11. Combined $\mathcal{A}_\tau$ and $\mathcal{A}_e$ results with statistical and systematic uncertainties for the 1990-1995 data. The pion inclusive channel is highly correlated with the hadronic channels

Channel	$\mathcal{A}_\tau$ (%)	$\mathcal{A}_e$ (%)
hadron	$15.35 \pm 0.96 \pm 0.50$	$16.32 \pm 1.27 \pm 0.09$
rho	$13.75 \pm 0.78 \pm 0.42$	$14.85 \pm 1.03 \pm 0.06$
a1(3h)	$14.89 \pm 1.50 \pm 1.05$	$14.68 \pm 1.98 \pm 0.40$
a1(h2π^0)	$16.14 \pm 1.74 \pm 1.44$	$14.13 \pm 2.30 \pm 0.42$
electron	$14.11 \pm 2.18 \pm 0.84$	$15.38 \pm 2.92 \pm 0.77$
muon	$14.05 \pm 2.07 \pm 0.82$	$11.91 \pm 2.71 \pm 0.17$
acollinearity	$13.34 \pm 3.83 \pm 1.80$	$19.41 \pm 5.02 \pm 0.24$
pion inclusive	$14.93 \pm 0.83 \pm 0.87$	$14.91 \pm 1.11 \pm 0.17$

Table 12. Combined $\mathcal{A}_e$, $\mathcal{A}_\tau$ and $\mathcal{A}_{e-\tau}$ results with statistical and systematic uncertainties for the 1990-1995 data

$\mathcal{A}_\tau$ (%)	$14.51 \pm 0.52 \pm 0.29$
$\mathcal{A}_e$ (%)	$15.04 \pm 0.68 \pm 0.08$
$\mathcal{A}_{e\text{-}\tau}$ (%)	$14.74 \pm 0.41 \pm 0.18$

7 Discussion

The $\mathcal{A}_\tau$ and $\mathcal{A}_e$ parameters are measured by means of similar methods by the three other LEP collaborations

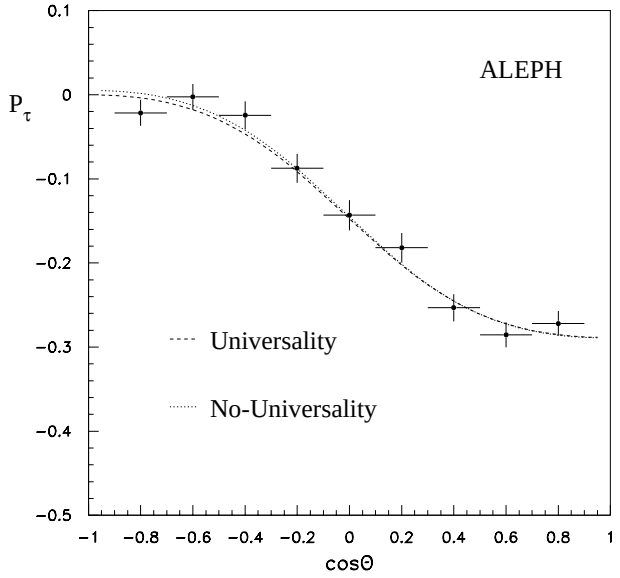

Fig. 26. Polarisation dependence on $\cos\theta$ for the LEP I data. The curves corresponding to (1) for parameters given by fits with (dashed line) and without (dotted line) the universality constraint are superimposed

Table 13. Effective lepton vector and axial vector couplings

g_V^e	-0.0384 ± 0.0015	g_A^e	-0.50171 ± 0.00056
g_V^μ	-0.0377 ± 0.0055	g_A^μ	-0.50043 ± 0.00094
g_V^τ	-0.0367 ± 0.0015	g_A^τ	-0.50219 ± 0.00093
g_V^l	-0.03747 ± 0.00096	g_A^l	-0.50155 ± 0.00045

[27–29]. The $\mathcal{A}_e$ asymmetry is also measured by the SLD collaboration [30] using the beam polarisation.

All the results are shown in Fig. 27a where a reasonable general agreement can be observed.

The $\mathcal{A}_\tau$, $\mathcal{A}_e$, and A_{fb}^0 asymmetries at the Z pole are related by the equations:

$$A_{fb}^{0,e} = \frac{3}{4}(\mathcal{A}_e)^2 \ , \qquad A_{fb}^{0,\tau} = \frac{3}{4}\mathcal{A}_e\mathcal{A}_\tau \ . \tag{12}$$

The comparison of the present measurements of $\mathcal{A}_e$ and $\mathcal{A}_\tau$ with the forward-backward asymmetries measured by the ALEPH collaboration [11] is presented in Fig. 27b.

Assuming universality, the leptonic forward-backward asymmetry measured by ALEPH, using all the leptonic Z decay channels, is $A_{fb}^{0,l} = 0.0173 \pm 0.0016$ [11], to be compared with $\frac{3}{4}(\mathcal{A}_{e\text{-}\tau})^2 = 0.0163 \pm 0.0010$.

The information given by the τ polarisation measurement can be used, together with the forward-backward asymmetries and the partial widths of the Z decays into lepton pairs [11], to determine the Z leptonic couplings. The results obtained by the procedure of [11] are given in Fig. 28 and Table 13.

Comparing these numbers with the values of the couplings presented in [11] shows the important weight of the τ polarisation measurement in the Z leptonic coupling determination.

8 Conclusion

From the $\mathcal{A}_\tau$ and $\mathcal{A}_e$ values obtained through the τ polarisation measurement:

$$\mathcal{A}_\tau = 0.1451 \pm 0.0059 \ , \qquad \mathcal{A}_e = 0.1504 \pm 0.0068 \ ,$$

the following ratios of the effective couplings are computed:

$$g_V^\tau/g_A^\tau = 0.0729 \pm 0.0030 \ ,$$
$$g_V^e/g_A^e = 0.0756 \pm 0.0035 \ ,$$
$$\frac{g_V^\tau/g_A^\tau}{g_V^e/g_A^e} = 0.964 \pm 0.060 \ .$$

The universal value

$$\mathcal{A}_{e\text{-}\tau} = 0.1474 \pm 0.0045$$

translates into a determination of the effective weak mixing angle

$$\sin^2\theta_{\rm W}^{\rm eff} = 0.23147 \pm 0.00057 \ . \tag{13}$$

Using both the τ polarisation and the leptonic forward-backward asymmetries measured by ALEPH, the value

$$\sin^2\theta_{\rm W}^{\rm eff} = 0.23130 \pm 0.00048 \tag{14}$$

is obtained.

Acknowledgements. We wish to express our thanks to our colleagues from the accelerator divisions for the excellent performance of LEP. We also thank the engineers and support personnel at our home institutions for contributing to the success of ALEPH. Those of us who are guests at CERN thank the laboratory for its hospitality and support.

A Tau direction estimator

A.1 The ideal case

First consider the case of a τ event where both τ's decay into a single pion with momentum vector measured perfectly (Fig. 29). Let T_0 be the interaction point and $\mathrm{H}_\pm$ points on each reconstructed track, in the vicinity of the decay points. The vectors $\hat{h}^\pm$ and $\hat{\tau}^\pm$ are unit vectors along the $\pi^\pm$ and $\tau^\pm$ momenta respectively, $l_\pm$ are the $\tau^\pm$ decay lengths and $\delta_\pm$ the distances of $\mathrm{H}_\pm$ to the $\tau^\pm$ decay points. From $\hat{\tau}^+ = -\hat{\tau}^-$ and the relation (Fig. 29)

$$\overrightarrow{\mathrm{OT}}_0 + l_\pm\hat{\tau}^\pm = \overrightarrow{\mathrm{OH}}_\pm + \delta_\pm\hat{h}^\pm \ ,$$

where O is an arbitrary origin, the equation

$$l\hat{\tau} = \delta_-\hat{h}^- - \delta_+\hat{h}^+ + \overrightarrow{\mathrm{H_+H_-}} \tag{15}$$

follows, where $l = l_+ + l_-$ and $\hat{\tau} = \hat{\tau}^-$.

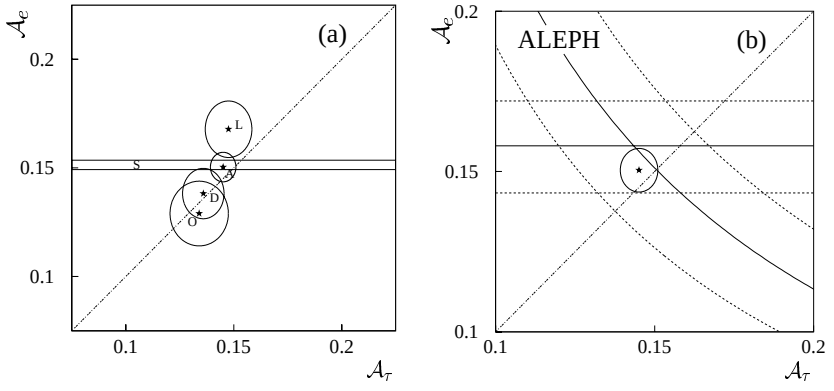

Fig. 27. **a** Comparison of the $\mathcal{A}_e$ and $\mathcal{A}_\tau$ measurements by the ALEPH (A), DELPHI (D), L3 (L), and OPAL (O) collaborations. The ellipses are one standard error contours (39% CL). The horizontal lines represent the SLD (S) $\mathcal{A}_e$ measurement through the left-right asymmetry of the cross-sections plus and minus one standard deviation. **b** Comparison of ALEPH $\mathcal{A}_\tau$, $\mathcal{A}_e$, and A^0_{fb} measurements. The ellipse is the one standard error contour. The hyperbolas and horizontal lines represent the $A^{0,\tau}_{fb}$ and $A^{0,e}_{fb}$ measurements respectively (plus and minus one standard error)

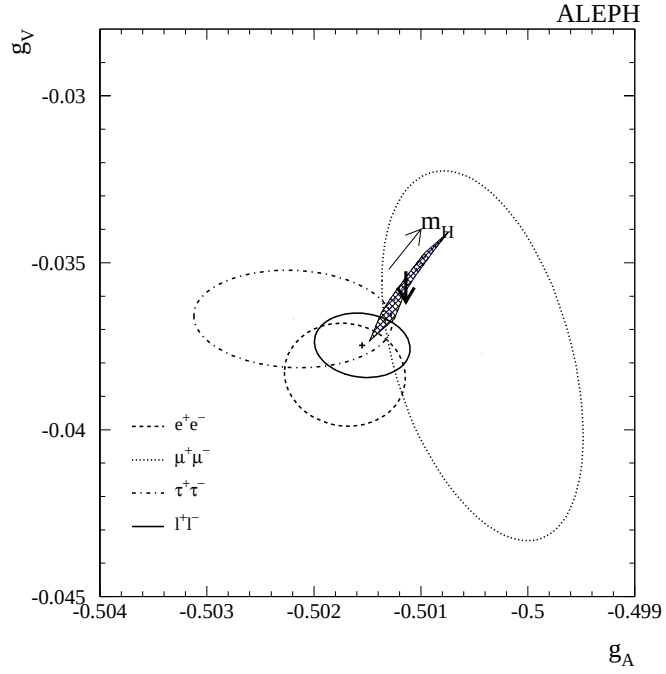

Fig. 28. Effective lepton couplings. The ellipses are one standard deviation contours (39% CL). The shaded area indicates the Standard Model expectation for $M_{\rm t} = 174 \pm 5$ Gev/c^2 and $90 < M_{\rm H}\,({\rm GeV}/c^2) < 1000$; the vertical arrow shows the change if the electromagnetic coupling constant is varied within its error

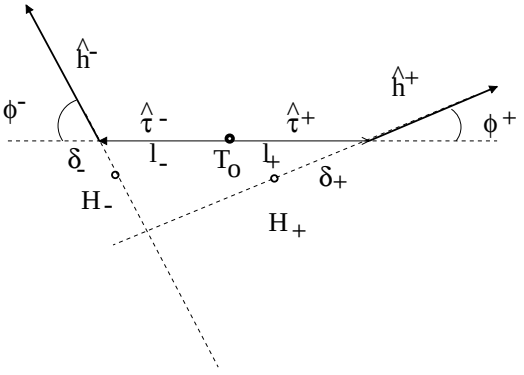

Fig. 29. Decay of a τ pair

Taking for $H_\pm$ the end points of the vector $\vec{D}_h$ defined [6][1] as the minimum approach vector between the two reconstructed tracks, the previous equation becomes

$$l\hat{\tau} = l\vec{A}_h + \vec{D}_h \ , \tag{16}$$

where the vector $\vec{D}_h$ is orthogonal to the hadronic plane spanned by $\hat{h}^+$ and $\hat{h}^-$ and the vector $\vec{A}_h$ lies in this plane.

The angles $\phi^\pm$ (Fig. 29) are given by (9),

$$\cos\phi^\pm = \frac{2E_{\tau^\pm}E_{h^\pm} - m_\tau^2 - m_{h^\pm}^2}{2p_{\tau^\pm}p_{h^\pm}} \ ,$$

consequence of the τ mass constraint, where E, p, and m are energy, momentum, and mass of τ's and hadrons (π's).

[1] A similar analysis of the ideal case is given in [31]

Accordingly, the two kinematically found τ^- directions, defined by the unit vectors $\hat{\tau}_1$ and $\hat{\tau}_2$, are the intersections of two cones having $-\hat{h}^+$ and $\hat{h}^-$ for axes and $\phi^\pm$ for opening angles. The vector $\hat{\tau}_1 + \hat{\tau}_2$ lies then in the hadronic plane and is, therefore, orthogonal to $\vec{D}_h$ (Fig. 30). This implies

$$\vec{D}_h \cdot \hat{\tau}_1 = -\vec{D}_h \cdot \hat{\tau}_2 \ . \tag{17}$$

The vector $\vec{A}_h$, projection of $\hat{\tau}$ on the hadronic plane, is the internal bisector of $\hat{\tau}_1$ and $\hat{\tau}_2$. These properties, with (16), lead to

$$l = \frac{|\vec{D}_h|}{\sqrt{1 - |\vec{A}_h|^2}} \ ,$$

since l is, by definition, a positive length. The positivity of l and (16) and (17) imply that the physical τ direction is determined by the relation

$$\vec{D}_h \cdot \hat{\tau}_{\rm true} \geq 0 \ . \tag{18}$$

For hemispheres with a 3-prong decay, the vector $\hat{h}^\pm$ is defined as equal to the sum of the three momenta and originating from the 3-track common vertex.

A.2 The general case

When π^0's are produced, the vector $\vec{A}_h$, which is kinematically determined, is still measurable, but the exact

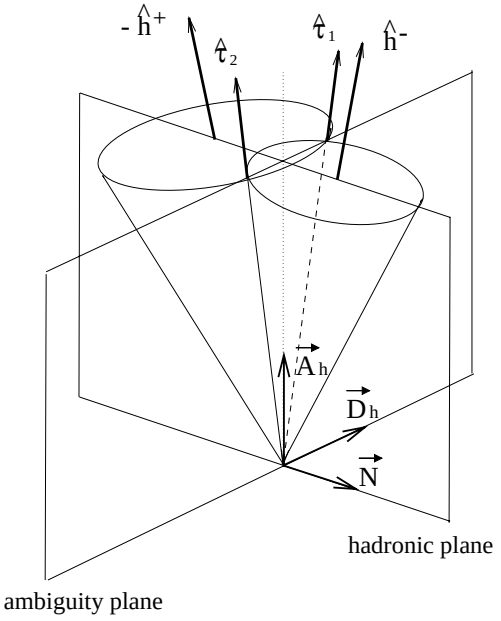

Fig. 30. Definition of vectors $\vec{A}_h$, $\vec{D}_h$, and $\vec{N}$

reconstruction of $\vec{D}_h$ given in the previous section is not possible and an approximation must be made.

The vectors $\hat{h}^{\pm}$ are now unit vectors along the sums of the hadron momenta in each hemisphere. Two vectors, which make with $\vec{A}_h$ an orthogonal system, can be unambiguously measured:

$$\vec{h}_\perp = \hat{h}^- \times \hat{h}^+ \ ,$$

which is normal to the hadronic plane, and

$$\vec{N} = \hat{h}_\perp \times \hat{\tau} = \hat{h}^+ \cos\phi^- + \hat{h}^- \cos\phi^+ \ ,$$

which is normal to the ambiguity plane spanned by $\hat{\tau}_1$ and $\hat{\tau}_2$. In terms of $\vec{h}_\perp$ and $\vec{N}$, the analytical expressions of $\vec{A}_h$ and $\vec{D}_h$ are

$$\vec{A}_h = \vec{N} \times \vec{h}_\perp \,/\, \vec{h}_\perp^{\,2} \ ,$$
$$\vec{D}_h = \vec{h}_\perp \,(\overrightarrow{\Delta \mathrm{H}} \cdot \vec{h}_\perp) \,/\, \vec{h}_\perp^{\,2} \ .$$

The vector $\overrightarrow{\Delta \mathrm{H}}$ is equal to $\overrightarrow{\mathrm{H_+H_-}}$, where $\mathrm{H}_\pm$ are arbitrary points on the lines drawn along the vectors $\hat{h}^{\pm}$ from the $\tau^{\pm}$ decay points, lines which coincide with the reconstructed tracks in the ideal case of the previous section.

The charged tracks reconstructed in each hemisphere are used to define an approximation of $\vec{D}_h$. Let $\hat{c}^{\pm}$ be unit vectors along the momenta of the charged particles, $\mathrm{C}_\pm$ points on the charged tracks in the neighbourhood of the decay points, $\vec{c}_\perp = \hat{c}^- \times \hat{c}^+$, and $\overrightarrow{\Delta \mathrm{C}} = \overrightarrow{\mathrm{C_+C_-}}$. If the vectors $\hat{c}_\perp$ and $\hat{h}_\perp$ are collinear, the space planes parallel to the hadronic plane and containing the $\tau^{\pm}$ decay points contain also the charged tracks. The vector $\vec{D}_h$ is then equal to the minimum approach vector between the charged tracks. In the most general case, an equation similar to (16) can be written [6]:

$$l\hat{\tau} = l\vec{A}_c + \vec{D}_c \ , \qquad (19)$$

where the vector $\vec{D}_c$, whose length is proportional to the minimum distance between the charged tracks, is collinear to $\vec{h}_\perp$:

$$\vec{A}_c = \vec{N} \times \vec{c}_\perp \,/\, (\vec{h}_\perp \cdot \vec{c}_\perp) \ ,$$
$$\vec{D}_c = \vec{h}_\perp \,(\overrightarrow{\Delta \mathrm{C}} \cdot \vec{c}_\perp) \,/\, (\vec{h}_\perp \cdot \vec{c}_\perp) \ .$$

As the relation (16) is still true, the expression of the $\vec{D}_h$ vector can be written as:

$$\vec{D}_h = \vec{D}_c + l\,(\vec{A}_c - \vec{A}_h) \ . \qquad (20)$$

In the (20), the vectors $\vec{D}_c$, $\vec{A}_c$, and $\vec{A}_h$ are measurable, but the decay length remains unknown. Taking the mean τ decay length sum $\bar{l} = 4.6$ mm as a value for l, an approximation of $\vec{D}_h$, denoted $\vec{D}_{h_{\mathrm{eff}}}$, is obtained.

The vector $\vec{A}_c$ lies in the ambiguity plane and, since both $\vec{D}_h$ and $\vec{D}_c$ are collinear to $\vec{h}_\perp$, the projection of $l\vec{A}_c$ on $\vec{A}_h$ is $l\vec{A}_h$, analytically $\vec{A}_c \cdot \vec{A}_h = \vec{N}^2/\vec{h}_\perp^{\,2} = \vec{A}_h^2$. Therefore, the vector $\vec{D}_{h_{\mathrm{eff}}}$ is proportional to $\vec{D}_h$, irrespectively of the value of $\bar{l}$. As in the ideal case,

$$\vec{D}_{h_{\mathrm{eff}}} \cdot \hat{\tau}_1 = -\vec{D}_{h_{\mathrm{eff}}} \cdot \hat{\tau}_2 \ , \qquad (21)$$

and the τ direction giving the positive value for $\vec{D}_{h_{\mathrm{eff}}} \cdot \hat{\tau}$ can be selected.

Because of the approximation made when π^0's are present and resolution effects, this selected direction is only correct on a statistical basis and probabilities, computed from reference distributions of $\vec{D}_{h_{\mathrm{eff}}} \cdot \hat{\tau}$, are assigned to the two solutions.

References

1. ALEPH Collaboration, Measurement of the polarization of τ leptons produced in Z decays, Phys. Lett. B **265** (1991) 430
2. ALEPH Collaboration, Measurement of the tau polarisation at the Z resonance, Z. Phys. C **59** (1993) 369
3. ALEPH Collaboration, Improved tau polarisation measurement, Z. Phys. C **69** (1996) 183
4. D. Bardin et al., Z. Phys. C **44** (1989) 493; Comp. Phys. Comm. **59** (1990) 303; Nucl. Phys. B **351** (1991) 1; Phys. Lett. B **255** (1991) 290; CERN-TH 6443-92 (May 1992) and hep-ph/9412201; ZFITTER v.6.10 A Semi-Analytical Program for Fermion Pair Production in e^+e^- Annihilation, DESY 99-070, June 1999
5. M. Davier, L. Duflot, F. Le Diberder, A. Rougé, Phys. Lett. B **306** (1993) 411
6. ALEPH Collaboration, Measurement of the τ lepton lifetime with the three-dimensional impact parameter method, Z. Phys. C **74** (1997) 387
7. D.E. Groom et al. (Particle Data Group), Eur. Phys. J. C **15** (2000) 1
8. J.H. Kühn, E. Mirkes, Z. Phys. C **56** (1992) 661; C **67** (1995) 364 (erratum)
9. ALEPH Collaboration, ALEPH: A detector for electron-positron annihilation at LEP, Nucl. Instrum. Methods A **294** (1990) 121

10. ALEPH Collaboration, Performance of the ALEPH detector at LEP, Nucl. Instrum. Methods A **360** (1995) 481
11. ALEPH Collaboration, Measurement of the Z Resonance Parameters at LEP, Eur. Phys. J. C **14** (2000) 1
12. S. Jadach, Z. Wąs, Comp. Phys. Comm. **66** (1991) 276
13. H. Anlauf, et al. Comp. Phys. Comm. **79** (1994) 466
14. M. Böhm, A. Denner, W. Hollik, Nucl. Phys. B **304** (1998) 687; F.A. Berends, R. Kleiss, W. Hollik, Nucl. Phys. B **304** (1998) 712; Computer program BABAMC, courtesy of R. Kleiss
15. J.A.M. Vermaseren, in Proceedings of the IV International Workshop on Gamma Gamma Interactions, eds. G. Cochard, P. Kessler (1980)
16. J.M. Hilgart, R. Kleiss, F. Le Diberder, Comp. Phys. Comm. **75** (1993) 191
17. ALEPH Collaboration, Tau hadronic branching ratios, Z. Phys. C **70** (1996) 579
18. ALEPH Collaboration, A study of τ decays involving η and ω mesons Z. Phys. C **74** (1997) 263
19. ALEPH Collaboration, Tau leptonic branching ratios, Z. Phys. C **70** (1996) 561
20. ALEPH Collaboration, Measurement of the Spectral Functions of Vector Current Hadronic Tau Decays, Z. Phys. C. **76** (1997) 15
21. ALEPH Collaboration, Measurement of the Spectral Functions of Axial-Vector Hadronic τ Decays and Determination of $\alpha_S(M_\tau^2)$, Eur. Phys. J. C. **4** (1998) 409
22. ALEPH Collaboration, Measurement of Tau Branching Ratios, Z. Phys. C **54** (1992) 211
23. R. Alemany, N. Rius, J. Bernabeu, J.J. Gomez-Cadenas, A. Pich, Nucl. Phys. B **379**, (1992) 3
24. T. Sjöstrand, Comp. Phys. Comm., **82** (1994) 74
25. ALEPH Collaboration, K^0 production in one-prong τ decays, Phys. Lett. B **332** (1994) 219; One-prong τ decays with kaons, Eur. Phys. J. C. **10** (1999) 1
26. I. Nikolic, Thesis, Université de Paris-Sud, Orsay, LAL 96-27 (1996)
27. OPAL Collaboration, A Precise Measurement of the Tau Polarization and its Forward-Backward Asymmetry at LEP, Z. Phys. C **72** (1996) 365
28. L3 Collaboration, Measurement of τ Polarisation at LEP, Phys. Lett. B **429** (1998) 387
29. DELPHI Collaboration, A Precise Measurement of the τ Polarisation at LEP-1, Eur. Phys. J. C **14** (2000) 585
30. SLD Collaboration, A High-Precision Measurement of the Left-Right Z Boson Cross-Section Asymmetry, Phys. Rev. Lett. **84** (2000) 5945
31. J.-H. Kühn, Phys. Lett. B **313** (1993) 458